University of Plymouth

PEARL **https://pearl.plymouth.ac.uk**

Faculty of Science and Engineering | School of Engineering, Computing and Mathematics

2020-02

Validation of a CFD-based numerical wave tank model for the power production assessment of the wavestar ocean wave energy converter

Windt, C

http://hdl.handle.net/10026.1/14795

10.1016/j.renene.2019.08.059
Renewable Energy
Elsevier

All content in PEARL is protected by copyright law. Author manuscripts are made available in accordance with publisher policies. Please cite only the published version using the details provided on the item record or document. In the absence of an open licence (e.g. Creative Commons), permissions for further reuse of content should be sought from the publisher or author.

Validation of a CFD-based numerical wave tank model for the power production assessment of the Wavestar ocean wave energy converter

Christian Windt[a,*], Josh Davidson[c], Edward J. Ransley[b], Deborah Greaves[b], Morten Jakobsen[d], Morten Kramer[d], John V. Ringwood[a]

[a] *Centre for Ocean Energy Research, Maynooth University, Co. Kildare, Ireland*
[b] *School of Engineering, Plymouth Univeristy, UK*
[c] *Department of Fluid Mechanics, Faculty of Mechanical Engineering Budapest University of Technology and Economics, Hungary*
[d] *Department of Civil Engineering, Aalborg University, Denmark*

Abstract

CFD-based numerical wave tank (CNWT) models, are a useful tool for the analysis of wave energy converters (WECs). During the development of a CNWT, model validation is vital, to prove the accuracy of the numerical solution. This paper presents an extensive validation study of a CNWT model for the 1:5 scale Wavestar point-absorber device. The previous studies reported by Ransley et al. [1] and Windt et al. [2] are extended in this paper, by including cases in which the power-take off (PTO) system is included in the model. In this study, the PTO is represented as a linear spring-damper system, providing a good approximation to the full PTO dynamics. The spring stiffness and damping coefficients in the numerical PTO model are determined through a linear least squares fit of the experimental PTO position, velocity and force data. The numerical results for free surface elevation, PTO data (position, velocity, force), generated power and pressure on the WEC hull are shown to compare well with the experimental measurements.

Keywords: **Numerical wave tank; validation; Wavestar; OpenFOAM; RANS**

*Corresponding author
Email address: christian.windt.2017@mumail.ie (Christian Windt)

Nomenclature

Abbreviations

CFD	Computational Fluid Dynamics
CNWT	CFD-based numerical wave tank
CoM	Centre of mass
CPH	Cells per wave height
CPL	Cells per wave length
DoF	Degree of freedom
Exp	Identifier for experimental results
FSE	Free surface elevation
MULES	Multi-Dimensional Limiter for Explicit Solutions
NRMSE	Normalised root mean squared error
Num	Identifier for numerical results
NWM	Numerical wave maker
PF	Potential flow
PG	Pressure gauge
PISO	Pressure-implicit split-operator
PIV	Particle image velocimitry
PTO	Power take-off
PWT	Physical wave tank
RANS	Reynolds averaged Navier-Stokes
SIMPLE	Semi-implicit method for pressure-linked equations
TRL	Technology readiness level
WEC	Wave energy converter
WP	Wave probe
WSI	Wave-structure interaction

Greek letters

α	Angle to the piston attachment arm
α_{VF}	Water volume fraction
β	Angle to the reference point
γ	Angle to the device arm
λ	Wave length
ω	Angular velocity
Φ	Specific fluid quantity
φ	State vector
ρ	Fluid density
σ	Standard deviation
τ	Power take-off torque
Θ	Device rotational angle
θ	Angle between device arm and reference point
ξ	Damping and stiffness matrix
$\hat{\xi}$	Estimated damping and stiffness matrix

Roman letters

a	Distance between pivot point and piston attachement point
b	Length of the piston attachment arm
D	Power take-off damping
d	Water depth
Δt	Time step
F_{PTO}	Power take-off Force
$\mathbf{f}_b$	External forces
H	Wave height
K	Power take-off stiffness
L_a	Absorption relaxation zone length
L_g	Generation relaxation zone length
N	Number of samples
p	Pressure
$\mathbf{T}$	Viscous stress tensor
T	Wave period
t	Time
$\mathbf{u}$	Velocity field
$\mathbf{u_r}$	Interface compression velocity
v_{PTO}	Linear power take-off velocity
Xc	Cylinder displacement
x_{PTO}	Linear power take-off displacement

1. Introduction

Numerical modelling of WECs using CNWTs has recently attracted increased attention [3]. The previously relatively slow computational performance of Computational Fluid Dynamics (CFD) simulations are gradually improving with modern computing resources. The main advantage of CNWTs is the ability to provide high-fidelity analysis of WEC performance, which can allow in-depth optimisation and performance assessment of a WEC design/concept at low Technology readiness levels (TRLs) and capital expenditure, as discussed in [4, 5].

1.1. Validation

It is well-known, in many branches of engineering, that the application of CFD relies heavily on both verification and validation [6, 7] to ensure the accuracy of the numerical results. Verification of CFD simulations embraces the quantification of spatial and temporal discretisation errors. Validation covers the comparison to reference data and should to be a part of every CNWT experiment. In the case of numerical WEC analysis, validation should consider cases where the PTO and control systems are acting on the WEC. In such cases, the WEC (1) experiences realistic operational conditions, and (2) when controlled for energy maximisation, and therefore resonating with the incident waves, will typically experience increased non-linear hydrodynamic behaviour [8]. Generally, four different validation strategies can be identified, in which CFD results are compared to:

- Analytical results: For example, comparing free surface elevation (FSE) and velocity data against wave theory results, as in [9]
- Potential Flow (PF) simulations: CFD results can be shown to converge on PF results as the amplitudes of wave and/or body motions approach zero, as shown in [10]
- Other CFD simulations: Comparing CFD against benchmark CFD results has the drawback of not actually checking for physical validity, however, such tests can be helpful to evaluate computational efficiency [11]
- Experimental data: This is the most prominent method, giving a direct comparison against measured physical reality, within the bounds of experimental error and wave tank fidelity. From the literature reviewed in [3] it can be seen that experimental data is typically only available from scale model testing in a physical wave tank (PWT). Therefore, validating a CNWT model against experimental data risks the danger of drawing false conclusions if not taking experimental inaccuracies and scaling issues into account [12].

1.2. Recent relevant literature

Hu et al. [13] perform comprehensive validation studies for extreme wave conditions, considering both wave-only and wave-structure interaction (WSI) cases and find maximum differences of 15% in the measured forces compared to experimental results. Mishra et al. [14] measure the radiation forces on the *WaveBob* device under different conditions. Correlation coefficients between 0.73 and 0.99 are found when comparing experimental and numerical results.

Palm et al. [15] identify the influence of physical model inaccuracies on CNWT model validation, for a novel coupled mooring analysis methodology. The authors identify inaccuracies due to manufacturing tolerances of physical models or material properties. Prasad et al. [16] details measurement uncertainties caused by the instrumentation, ranging from $\pm 1\%$ up to $\pm 2.23\%$. Similar ranges of measurement uncertainty are found in [17].

Providing high resolution data sets and visualisation, CFD enables the (mostly qualitative) comparison of the flow field with experimental data. Relevant examples can be found in [18] and [19], for the analysis of Oscillating Wave Surge Converters. Employing Particle Image Velocimetry (PIV), Schmitt et al. [18] highlights the complexity and potential inaccuracies of the experimental setup. Hence, comparisons between numerical and physical results in a quantitative manner are difficult to conduct. With a focus on vortex shedding, Wei et al. [19] find agreement between physical and numerical results.

1.3. The Wavestar WEC experiments

The experimental validation data set follows tests performed on a 1:5 scale model of the Wavestar WEC (see Figure 2), reported by Jakobsen et al. [20]. This data set is particularly useful for CNWT WEC model validation, since (1) Pressure data on the hull is recorded; (2) The 1:5 scale is larger than most PWT experiments, representing more realistic hydrodynamic and turbulence effects compared to an actual full-scale device [12]; (3) The hydraulic PTO system operates in different conditions: undamped, damped and reactively control.

Ransley et al. [1] used this data set for the validation of a CNWT model, for fixed body and undamped freely moving body cases. Windt et al. [2] validated different dynamic mesh motion methods in the OpenFOAM environment, by replicating the free-decay tests in the Wavestar experiments. This paper extends [1] and [2] by considering cases in which the hydraulic PTO system is actively engaged.

In addition to the requirement of modelling the effect of the PTO system on the WEC, including the controlled PTO also challenges the CNWT model by introducing increased nonlinear hydrodynamic effects compared to the free floating case [8, 21]. Figure 1 shows the operational space of a WEC under uncontrolled (black line) and controlled (red line) conditions. A drastic magnification of the operational space is caused by the implementation of control, implying increased nonlinear hydrodynamic effects. In this paper the effects of the PTO are implemented using a representative, spring-damper model. This acts as a stepping stone towards a high-fidelity wave-to-wire simulation of the

Wavestar device, using CFD for the hydrodynamics and a high-fidelity model (considering the hydraulics and electromagnetic generator) for the PTO system, as demonstrated in [5].

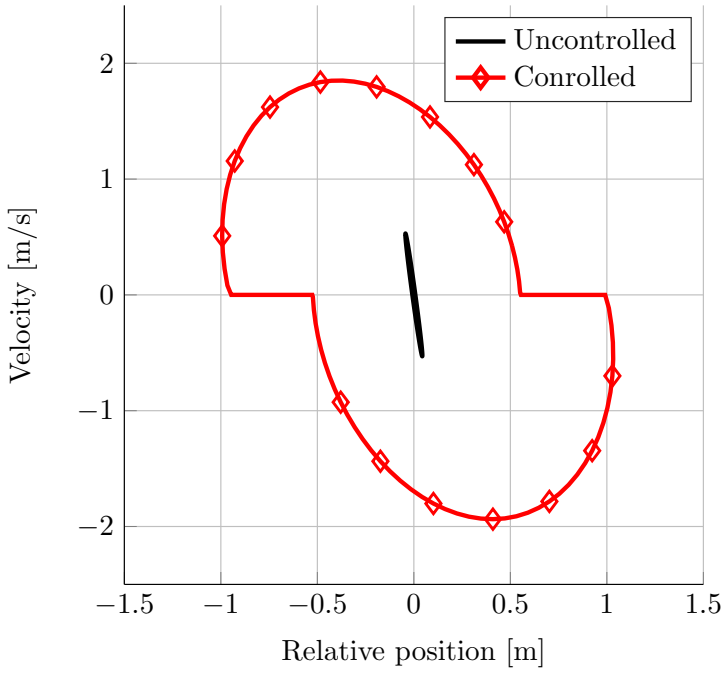

Figure 1: Operational space for a WEC with and without control applied (adapted from [21])

1.4. Outline of paper

The remainder of the paper is organised as follows. Section 2 introduces the experimental setup and WEC characteristics from the PWT test campaign. Section 3 describes the test cases considered in the validation study: wave-only simulation, wave diffraction and radiation tests, as well as wave-driven motion of the WEC with PTO damping. Section 4 shows the details of the CNWT used for the numerical simulations. Section 5 presents and discusses the results, while conclusions are drawn in Section 6.

2. Physical Wave Tank

The experimental data in this study originates from PWT tests of a 1:5 scale Wavestar model (see Figure 2), conducted at the Ocean Wave Basin at Plymouth University, detailed in [20] and [22]. A schematic of the experimental test setup, including significant dimensions, is depicted in Figure 3. System properties (mass, inertia, etc.) are listed in Table 1. The experimental data comprises:

- WEC motion : measured via the piston displacement in the hydraulic PTO cylinder (see Figure 3)
- PTO force : measured at the connection of the hydraulic PTO with the arm, using a single degree of freedom (DoF) load cell.
- Pressure on the WEC : measured at 29 locations on the hull, using pressure gauges (PGs) (see Figure 4 for PG numbering).
- FSE : measured at 16 locations in the tank, using wave probes (WPs) (see Figure 5 for WP numbering).

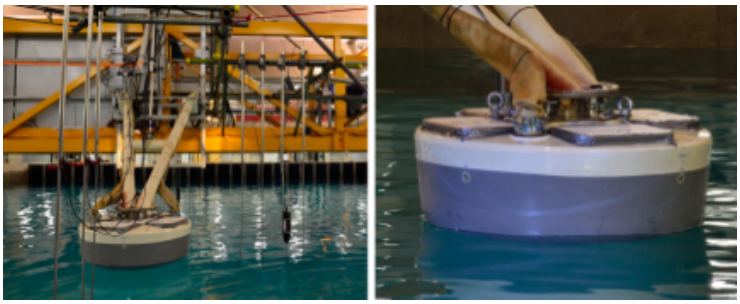

Figure 2: The 1:5 scale physical model of the Wavestar WEC in Plymouth Ocean Wave basin (adapted from [1])

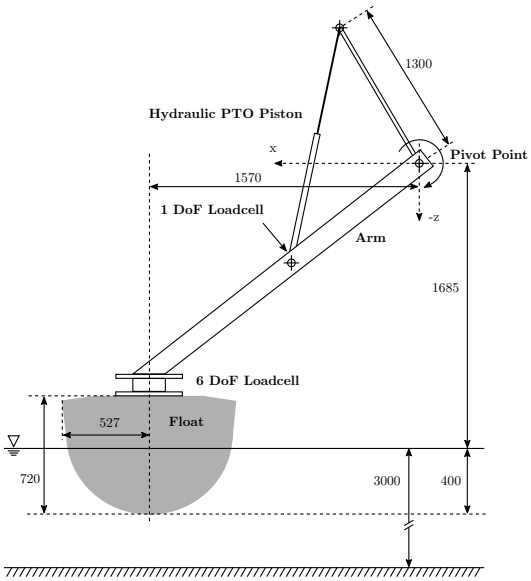

Figure 3: Schematic of the experimental setup, including the main dimensions (in mm). Schematic not to scale. (adopted from [20], [1])

Table 1: Physical properties of the 1:5 scale Wavestar model

Mass (Float & Arm)	220kg
Inertia	124kg m^2
Centre of Mass (CoM) of the floating system in equilibrium relative to the hinge position:	
x	1.3954m
y	0.0m
z	−1.3305m
Submergence (in equilibrium)	0.4m
Water depth d	3m

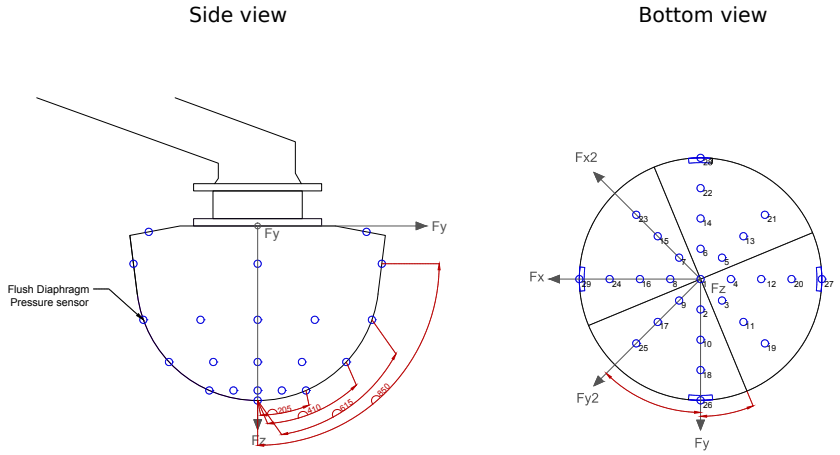

Figure 4: Pressure gauge locations on the WEC hull; distances in mm (adapted from [22])

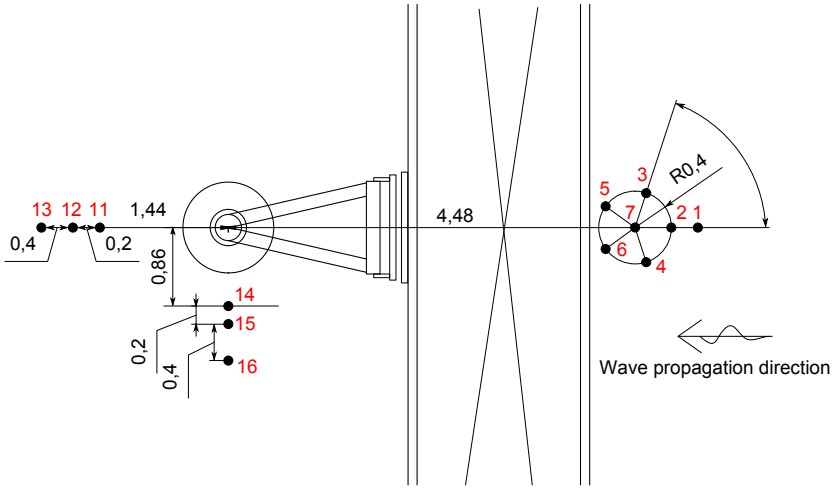

Figure 5: WP locations in the PWT; WPs numbered in red; distances in meters (adapted from [20])

3. Test Cases

Several different types of tests, each considering different types of waves, were conducted in the experimental PWT campaign. Sections 3.1-3.4 describe the test cases replicated in the CNWT, for the present validation study.

3.1. Waves-only

A waves-only test, without the WEC in the tank, is performed to benchmark the incident wave field. The present validation study considers this test case first to validate the numerical wave maker (NWM) and the wave propagation in the CNWT. A total of four different sea states are considered, MS01, MS02, MS03 and MS04, whose characteristics are listed in Table 2.

Table 2: Wave characteristics for monochromatic waves MS01, MS02, MS03 and MS04

			MS01	MS02	MS03	MS04
Wave height	H	[m]	0.1	0.15	0.25	0.25
Wave period	T	[s]	1.4	1.4	1.4	2.8
Wave length	λ	[m]	3.06	3.06	3.06	11.4
Wave steepness	H/λ	[-]	0.033	0.049	0.082	0.022

3.2. Wave Diffraction

In the diffraction tests, the WEC is held fixed in the tank, while subjected to incoming waves (MS01, MS02, MS03 and MS04). This test case is considered in the validation study to introduce WSI, without additionally including body motion at the same time, and thus reducing the WSI problem to wave diffraction only.

3.3. Wave Radiation

The wave radiation tests provide an initial validation of the WEC motion due to the PTO force. The wave radiation tests are conducted in a still tank with no input waves and the WEC motion is driven by a sinusoidal PTO force. Three cases are considered, with increasing PTO force amplitude and constant frequency, as listed in Table 3.

Table 3: Wave radiation test cases

	Frequency [Hz]	Period [s]	Amplitude [N]
DA300F35	0.35	2.86	300
DA400F35	0.35	2.86	400
DA600F35	0.35	2.86	600

3.4. WEC with PTO system

Finally, the full system is tested, with the WEC free to move, while subjected to incoming waves (MS01, MS02, MS03 and MS04) *and* PTO forces. Resistive control is employed, and different rotational PTO damping factors (D_{exp}) are considered in the PWT experiments, i.e. D_{exp} = 0, 50, 100 and 200N m s, which in theory lead to a PTO torque τ_{PTO}, following Equation (1), where the rotational spring stiffness K_{exp} is 0, due to the application of resistive control [23]. In the experimental setup, the PTO torque is transformed into a linear PTO force, applied through the hydraulic piston (see Figure 3).

$$\tau_{PTO} = D_{exp} \cdot \omega_{WEC} + K_{exp} \cdot \Theta_{WEC} \tag{1}$$

In Equation (1), ω_{WEC} is the angular velocity, and Θ_{WEC} the rotation angle around the pivot point (see Figure 3).

4. Numerical Wave Tank

The CNWT is implemented using the open-source CFD toolbox OpenFOAM [24]. More specifically, the OpenFOAM Foundation fork, version 4.1 [25], is employed. This study builds upon the work in Ransley et al. [1] and Windt et al. [2]; thus, these previous studies can provide useful guides for the CNWT setup used for the current validation tests.

4.1. Hydrodynamics

In OpenFOAM, the Reynolds averaged Navier-Stokes (RANS) equations, describing the conservation of mass (see Eq. (2)) and momentum (see Eq. (3)), are solved using the Finite-Volume method.

$$\nabla \cdot \mathbf{u} = 0 \tag{2}$$

$$\frac{\partial(\rho \mathbf{u})}{\partial t} + \nabla \cdot (\rho \mathbf{u}\mathbf{u}) = -\nabla p + \nabla \cdot \mathbf{T} + \rho \mathbf{f}_b \tag{3}$$

In equations (2) and (3), t represents time, $\mathbf{u}$ the fluid velocity, p the fluid pressure, ρ the fluid density, $\mathbf{T}$ the stress tensor and $\mathbf{f}_b$ external forces such as gravity.

In the employed CNWT, the PIMPLE algorithm [26] is used to solve the pressure-velocity coupling. PIMPLE blends the semi-implicit method for pressure-linked equations (SIMPLE) [27] and the pressure-implicit split-operator (PISO) [28] to achieve solutions for transient problems considering larger Courant numbers, allowing larger time steps.

To account for the two phase flow, the Volume of Fluid method, proposed in [29], is used, following:

$$\frac{\partial \alpha_{VF}}{\partial t} + \nabla \cdot (\mathbf{u}\alpha_{VF}) + \nabla \cdot [\mathbf{u_r}\alpha_{VF}(1-\alpha_{VF})] = 0 \tag{4}$$

$$\Phi = \alpha_{VF}\Phi_{\text{water}} + (1-\alpha_{VF})\Phi_{\text{air}}\,, \tag{5}$$

where α_{VF} denotes the volume fraction of water, $\mathbf{u_r}(t)$ is the relative velocity between the liquid and gaseous phases [30], and Φ is a specific fluid quantity, such as density. Boundedness of the transport equation is achieved through the Multi-Dimensional Limiter for Explicit Solutions (MULES) [31]. Following Eskilsson et al. [32], the free surface elevation is monitored by extracting the iso-surface of the volume fraction $\alpha_{VF} = 0.5$.

Laminar flow conditions are assumed for all simulations, as in [1]. The inclusion of turbulence modelling will be investigated in future work.

4.2. Body Motion

The body motion is solved using OpenFOAM's *sixDoFRigidBodyMotion* solver, which calculates the body's trajectory from the forces acting upon it, via Newton's 2nd law of motion. For this study, the WEC motion is constrained to the pitch DoF in the *sixDoFRigidBodyMotion* solver, and the angluar motion around the pivot point is calculated.

For the comparison with experimental data, the cylinder displacement $Xc(t)$ is calculated using geometrical transformations from the numerically measured translational displacement of the WEC. Defining a reference point on the WEC (red dot in Figure 6), whose location is tracked through the simulation, $Xc(t)$ is calculated following

$$\gamma(t) = \beta(t) - \theta \tag{6}$$

$$\alpha'(t) = \alpha + \gamma(t) \tag{7}$$

$$Xc(t) = \sqrt{-(cos(\alpha'(t)) \cdot 2 \cdot a \cdot b) - a^2 - b^2} \quad . \tag{8}$$

All relevant angles and distances are depicted in Figure 6, where time dependent variables are denoted with (t). From the x and z displacement of the reference point, $\beta(t)$ and subsequently $\gamma(t)$ and $Xc(t)$ are calculated.

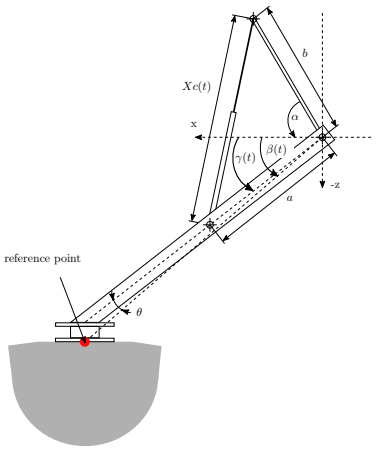

Figure 6: Relevant angles and distances for the calculation of the cylinder displacement $Xc(t)$, where time dependent variables are denoted with (t). The red dot represents the reference point, tracked throughout the simulation. From the x and z displacement of the reference point, $\beta(t)$ is calculated.

4.3. PTO Model

A preliminary study reported by the authors [33] attempted to approximate the PTO effects via an angular damper at the pivot point of the WEC, and thereby directly apply the theoretical PTO torque described by Equation 1. Although simple to implement, in the CNWT model, this approximation was found to be inadequate for replicating the dynamics of the system. Therefore, a more rigorous replication of the actual physical system is now implemented in the CNWT, whereby the PTO force acts on the WEC arm at the position of the 1 DoF loadcell (see Figure 3). The PTO force is modelled as a linear spring-damper system, which is defined in the *sixDoFRigidBodyMotion* solver via an anchor point, fixed throughout the simulation, and a reference point, moving with the body (position of the 1 DoF loadcell). The spring and damper forces are then calculated at each time step, multiplying user-defined spring (K_{num}) and damper (D_{num}) coeffients by the relative anchor-reference point displacement $x_{PTO}(t)$ and velocity $v_{PTO}(t)$, respectively (see Equation 9).

$$F_{PTO}(t) = D_{num} \cdot v_{PTO}(t) + K_{num} \cdot x_{PTO}(t) \tag{9}$$

Physically, $D_{num} \cdot v_{PTO}(t)$ describes the linear damping, applied to the WEC, via the hydraulic PTO piston. $K_{num} \cdot x_{PTO}(t)$ describes any reactive force applied through the PTO piston. In theory, for a resistively controller WEC, any reactive force should be zero. A more detailed discussion of the definition of the parameters D_{num} and K_{num} is given in Section 5.4.1.

4.4. Numerical Wave Maker

For numerical wave generation and absorption, the relaxation zone method, implemented in the *waves2Foam* toolbox [34], is employed. Generally, this

method requires larger domain sizes, thus longer computing times, compared to a static boundary NWM [35]. However, for the desired monochromatic sea state, preliminary studies revealed better accuracy for the *waves2Foam* wave maker, compared to the static boundary NWM *olaFOAM* [36]. To closely replicate the experimental conditions, no wave absorption is implemented in the y-direction, with solid concrete side walls present in the PWT (see Figure 8). Convergence studies, as presented in [35], were performed to determine the required wave generation relaxation zone length (L_g) and wave absorption relaxation zone length (L_a). The dimensions of the generation and absorption relaxation zone lengths are listed in Table 6. A screenshot of the NWT showing the mean water level, relaxation factor strengths and the WEC body, is depicted in Figure 8.

4.5. Boundary Conditions and Solution Schemes

The OpenFOAM specific boundary conditions for all domain boundaries (according to Fig. 7) are listed in Table 4. The OpenFOAM specific solution schemes for the temporal derivatives, gradients, divergence and the Laplace equation are listed in Table 5.

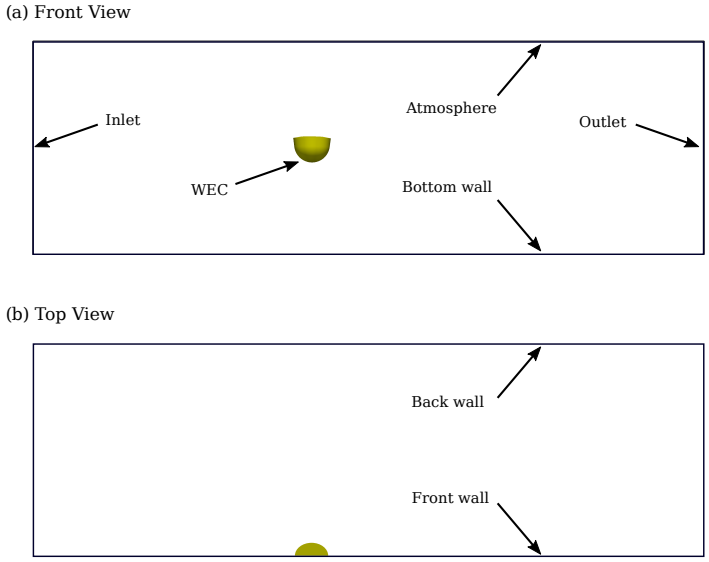

Figure 7: Labelling of the CNWT domain boundaries

Table 4: OpenFOAM boundary conditions in the CNWT; Asterisk marks *waves2Foam* specific boundary conditions

	U	p	*point displacement*	*alpha.water*
Back wall	*fixed Value* 0	*zeroGradient*	*fixed Value* 0	*zeroGradient*
Front wall	*symmetry*	*symmetry*	*symmetry*	*symmetry*
Bottom wall	*fixed Value* 0	*zeroGradient*	*fixed Value* 0	*zeroGradient*
Inlet	*waveVelocity**	*zeroGradient*	*fixed Value* 0	*waveAlpha**
Outlet	*fixed Value* 0	*zeroGradient*	*fixed Value* 0	*zeroGradient*
Atmosphere	*pressureInletOutletVelocity*	*totalPressure*	*fixed Value* 0	*inletOutlet*
WEC	*movingWallVelocity*	*zeroGradient*	*calculated*	*zeroGradient*

Table 5: OpenFOAM solution schemes in the CNWT

ddtSchemes	Euler
gradSchemes	*Gauss linear*
laplacianSchemes	*Gauss linear corrected*
divScheme U	*Gauss linear*
divScheme alpha	*Gauss interfaceCompression*

4.6. Discretisation

Following the convergence study outlined in [35], the spatial (in the free surface and near-body region) and temporal discretisations were determined. The spatial and temporal discretisations are listed in Table 6.

The spatial dimensions of the CNWT are 7.75m x (6.92m + 4λ) x 6m (WxLxH). A symmetry plane bisects the domain, to reduce the computational overhead, with the validity of exploiting symmetry in the CNWT for the Wavestar WEC being shown in [2]. The total cell count of the domain varies between 800k and 3M cells. A screen shot of the spatial discretisation in the interface and near-body region is depicted in Figure 9.

Table 6: Relaxations zone lengths and domain discretisation

Generation relaxation zone length (L_g)	1λ
Absorption relaxation zone length (L_a)	3λ
Reflection coefficient	2%
Spatial discretisation:	
dx	200CPL
dy	50CPL
dz	10CPH
Temporal discretisation	$1400\Delta t/T$

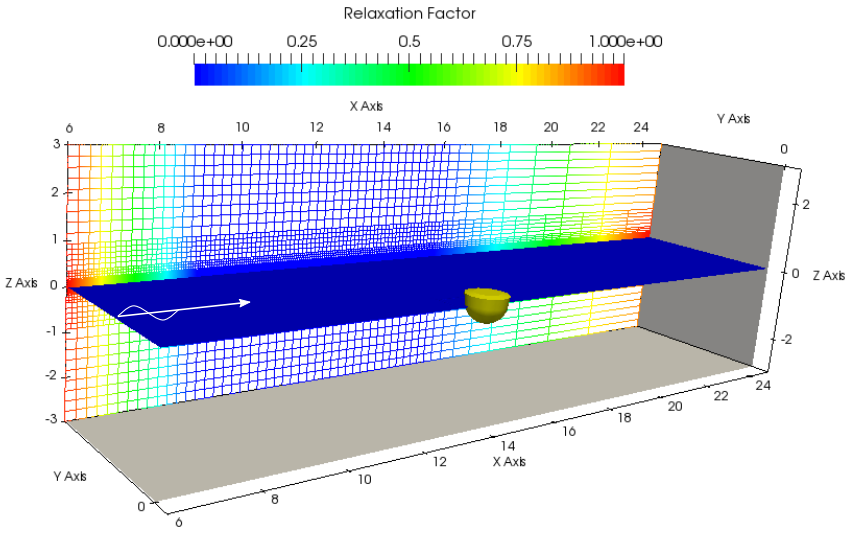

Figure 8: Visualisation of the relaxation strength, free surface and the buoy hull

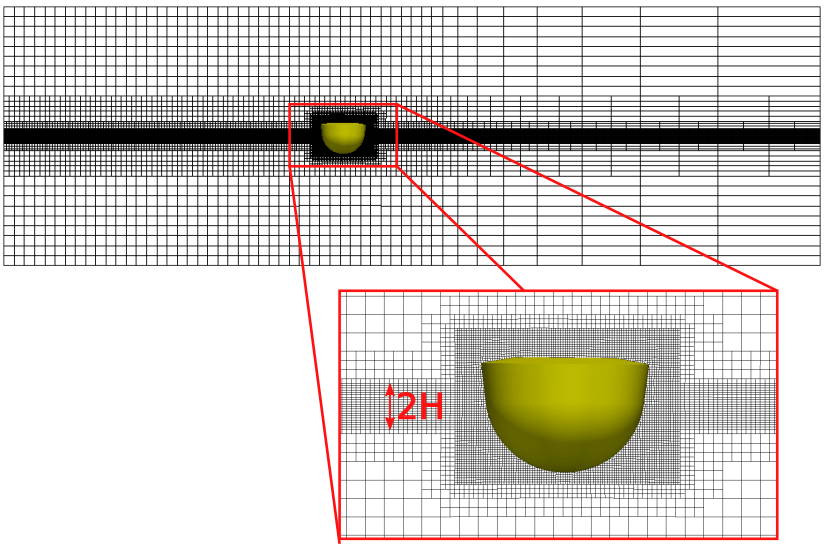

Figure 9: Spatial discretisation of the numerical domain with 10CPH and 200CPL. The discretisation is gradually refined towards the free surface interface. The finest discretisation of 10CPH and 200CPL stretches over one wave heights H below and above the still water line.

5. Results and Discussion

5.1. Waves-only

The generation and propagation of waves in the CNWT are validated first, comparing them to the wavefield using WP data. FSE data are compared at four WPs: 2, 7, 11 and 16, where WPs 2, 7 and 11 are aligned with the WEC center in the direction of wave propagation and WP16 is inline with the WEC, perpendicular to the wave propagation direction (see Figure 5).

5.1.1. Analysis

Phase averaged FSE time traces, from a zero-down crossing analysis, as in [35], are investigated, considering ten consecutive wave periods.

Firstly, the temporal scatter of the FSE is analysed, by calculating the standard deviation, σ, for the ten consecutive wave periods, at each WP. By way of example, Figure 10 shows the PWT phase-averaged mean FSE $\pm\sigma$ for sea state MS01. The results are listed in Table 7, showing that σ is relatively small for both the PWT and CNWT. These small, negligible values for σ are reflected by the indistinguishable lines in Figure 10. Comparing the PWT and the CNWT, the numerical results show standard deviations an order of magnitude smaller than in the PWT.

Table 7: FSE standard deviation for ten consecutive wave periods

PWT				
WP #	2	7	11	16
MS01 [m]	0.006	0.004	0.006	0.005
MS02 [m]	0.001	0.001	0.001	0.001
MS03 [m]	0.002	0.002	0.002	0.002
MS04 [m]	0.006	0.006	0.006	0.006
CNWT				
WP #	2	7	11	16
MS01 [m]	0.0007	0.0005	0.002	0.003
MS02 [m]	0.0001	0.0004	0.0006	0.0004
MS03 [m]	0.0005	0.0003	0.0017	0.001
MS04 [m]	0.0003	0.0004	0.0006	0.0005

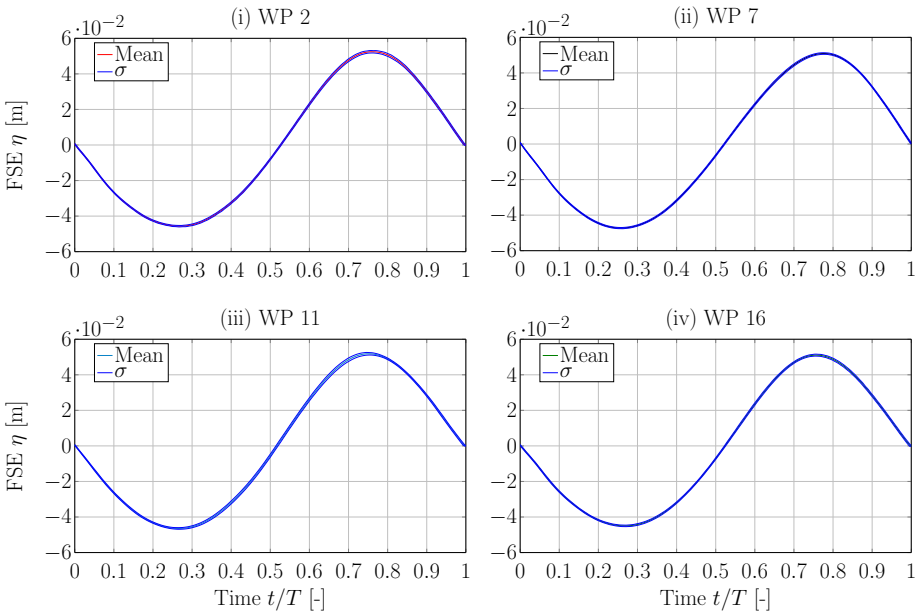

Figure 10: Mean FSE $\pm\sigma$ for sea state MS01 measured in the PWT

Next, the spatial scatter of the FSE is analysed, by comparing the three downwave WPs (7, 11 and 16) to WP2, which is the closest to the wavemaker. The comparison is quantified using the normalised root mean squared error (NRMSE), as defined in Equation (10), where y is the phase averaged FSE at WP2, $\hat{y}$ the phase averaged FSE at WP 7, 11 or 16 and N is the number of samples.

$$\text{NRMSE} = \sqrt{\frac{\sum(\hat{y}-y)^2}{N}} \cdot \frac{1}{\max(y)-\min(y)} \tag{10}$$

Ideally, the phase averaged FSE at the different WPs should match, resulting in a NRMSE of zero. However, due to effects such as (numerical) wave dissipation or reflections from the tank walls etc, some scatter between the WPs may be observed. The results are listed in Table 8 showing that the CNWT exhibits very little spatial scatter, suggesting relatively low numerical dissipation or reflections in the CNWT. In the PWT, larger spatial scatter can be observed, especially for sea states MS03 and MS04. This can likely be attributed to reflections from the end wall in the PWT.

Table 8: NRMSE of the phase averaged FSE compared to WP2

PWT				
WP #	2	7	11	16
MS01	–	0.0162	0.0163	0.0105
MS02	–	0.0138	0.0217	0.0173
MS03	–	0.0270	0.0160	0.0327
MS04	–	0.0187	0.0500	0.0580
CNWT				
WP #	2	7	11	16
MS01	–	0.0073	0.0098	0.0048
MS02	–	0.0192	0.0183	0.0181
MS03	–	0.0080	0.0075	0.0219
MS04	–	0.0019	0.0028	0.0025

Finally, the CNWT FSE data is directly compared against the PWT data. For a qualitative comparison, Figures 11 and 12 plot the mean phase averaged FSE of the CNWT and PWT at each WP, for the four different sea states. For a quantitative comparison, the NRMSE is calculated following Equation (10) (where y refers to the PWT data and $\hat{y}$ the CNWT data) and is listed in Table 9.

Overall good agreement between the numerical and experimental results is observed, with NRMSEs $\leq 6\%$. Particularly good agreement is found for the sea states with small wave heights, i.e. MS01 and MS02, with NRMSEs $\leq 2\%$. Increasing the wave height leads to larger deviation, i.e. NRMSEs $4-2\%$ for MS03 and $5-6\%$ for MS04. For sea state MS03, the main contribution for the deviation can be found at the wave crests. Similarly, for MS04, at WP 2 and 7, large deviation can be seen at the crests. At WP 11 and 15, deviations occur in both the crests and troughs.

Table 9: NRMSE between numerical and experimental FSE for wave-only cases

NRMSE [–]				
WP #	2	7	11	16
MS01	0.01	0.02	0.02	0.02
MS02	0.02	0.02	0.01	0.02
MS03	0.05	0.04	0.04	0.04
MS04	0.06	0.05	0.06	0.06

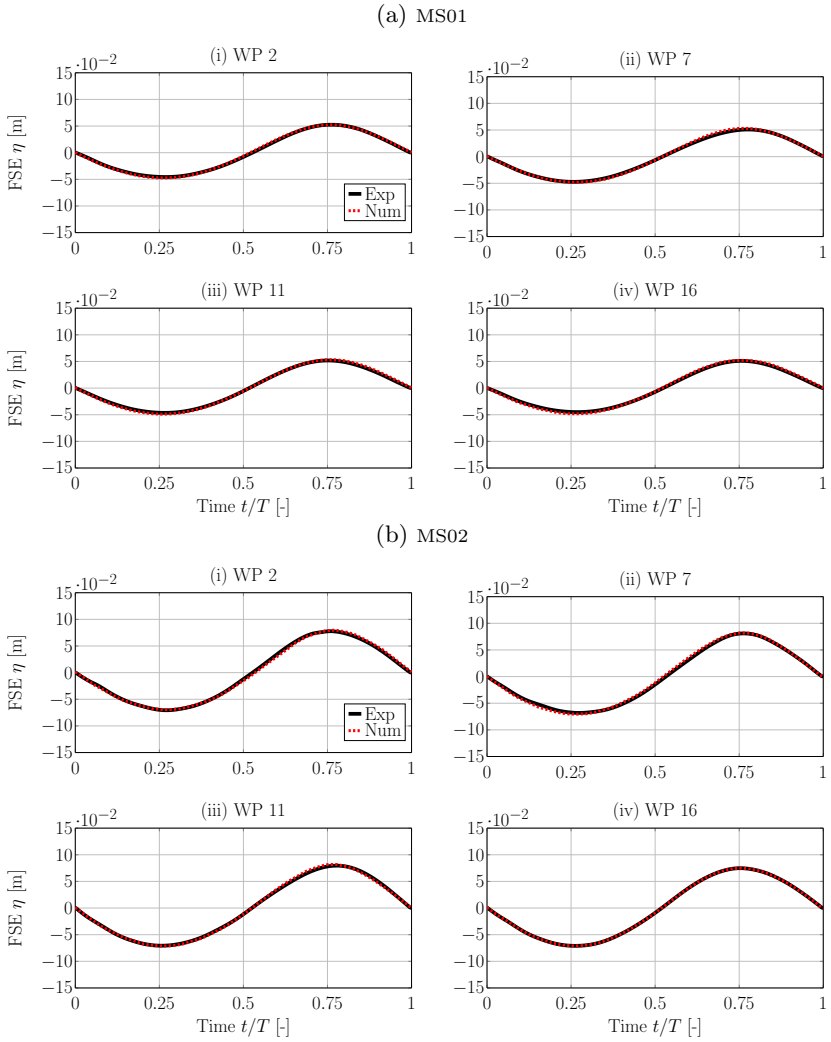

Figure 11: Mean phase averaged FSE for sea state MS01(a) and MS02 (b) at WP 2 (i), 7 (ii), 11 (iii), 16 (iv)

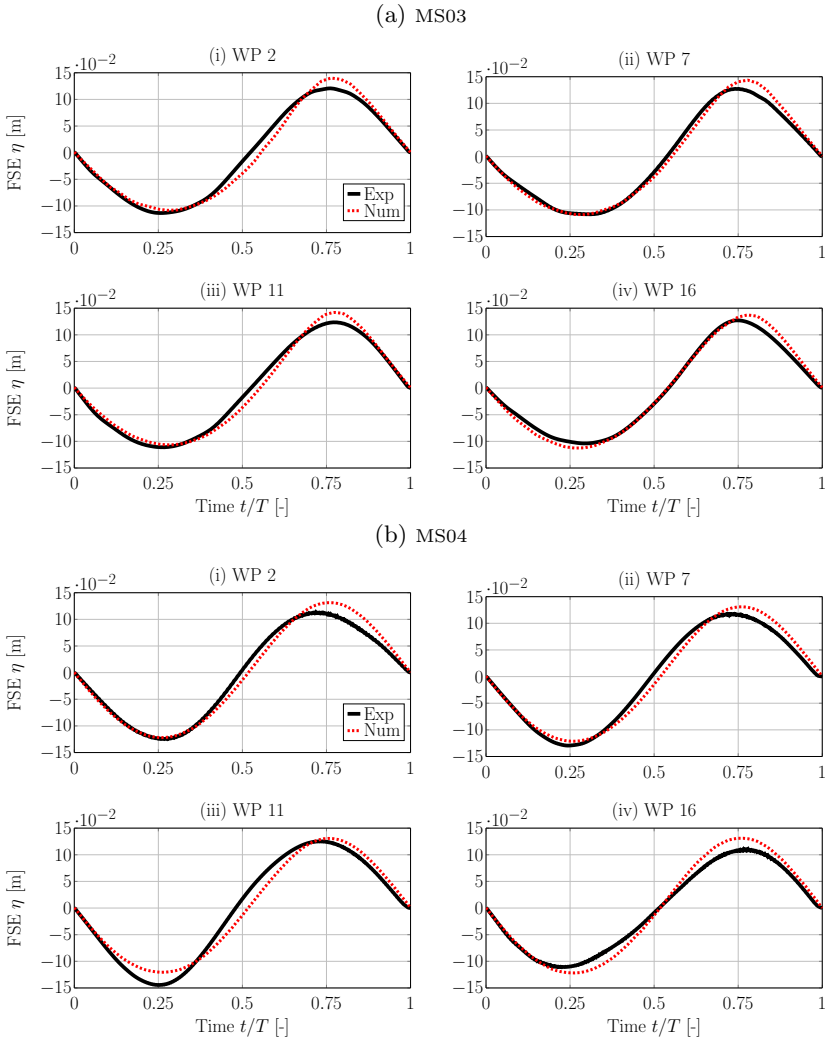

Figure 12: Mean phase averaged FSE for sea state MS03 (c) and MS04 (d) at WP 2 (i), 7 (ii), 11 (iii), 16 (iv)

For completeness, Figures 13 (a)–(d) show screen shots of the α_{VF} field (blue colour code for water, red colour code for air), and the velocity vectors in the computational domain. Clearly, from Figures 13 (a)–(c), an increased velocity can be observed with increased wave height. Furthermore, the influence of deep water and intermediate water conditions can be observed. While MS01–MS03 represent deep water conditions, large velocities can mostly be observed close to the free surface. In contrast, for sea state MS04, velocity vectors are significant almost throughout the entire water column.

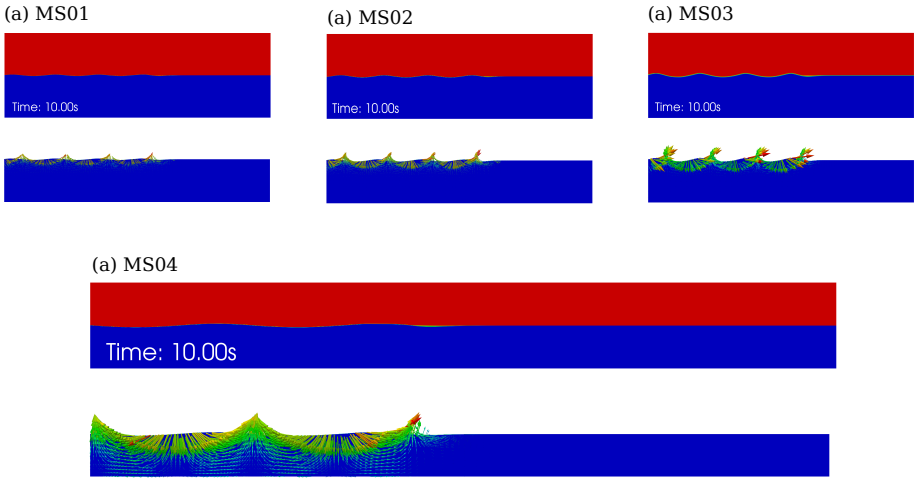

Figure 13: Screen shots of the computational domain showing the α_{VF} field (blue colour code for water, red colour code for air), and the velocity vectors

5.2. Wave Diffraction

The wave diffraction test case provides an initial validation of WSI, comparing the diffracted wave field, using WP data, and the fluid pressure on the WEC hull, using PG data. FSE data are compared at five WPs: 2, 11, 13, 14 and 16, where WPs 2, 11 and 13 are aligned with the centre of the WEC in wave propagation direction and WPs 14 and 16 are inline with the WEC, perpendicular to the wave propagation direction (see Figure 5). Pressure data are compared at four PGs: 1, 10, 14 and 12, where PG1 is located at the centre bottom, PG 10 on the downwave side, PG 12 on the centre side and PG14 on the upwave side (see Figure 4).

5.2.1. Analysis

For this case, the time traces are directly compared, rather than the phase averaged results, to show transient behaviour in the data, as the diffracted and incident wave fields interact with each other.

For a quantitative comparison, the NRMSE between the CNWT and PWT data is evaluated and listed in Table 10. Note that, for sea states MS01 and MS03, no experimental FSE data are available. For a qualitative comparison, time traces for the FSE and pressure, for sea states MS02 and MS04 are shown in Figures 14 - 17.

Comparing the FSE, good qualitative and quantitative agreement can be observed. Similar to the waves-only cases, MS02 shows better agreement (NRMSE$\leq$ 7%) than MS04 (NRMSE$\leq$ 11%). However, in both these sea states, marginally larger deviations compared to the waves-only cases can be seen. For sea state MS02, the larger deviation can potentially be attributed to the influence of reflections of the diffracted wave field from the side tank wall. Figure 18 depicts the wave field in the CNWT for sea state MS02 at a simulation time of 10s, showing diffracted waves travelling away from the WEC towards the tank wall. Similarly, Figure 19 shows the wave field in the CNWT for sea state MS04. Here, the effect of wave diffraction appears to be minimal. For this sea state, the mechanical constraints on the body motion could results in larger deviations. When attempting to hold the WEC fixed in the PWT, the wave force was transmitted to the supporting gantry which began to shake significantly and large vibrations could be observed in both the WEC and the WPs (which are all attached to the gantry). This parasitic influence of the supporting restraints in the PWT is obviously not modelled in the CNWT, where a perfectly stationary body and WPs are assumed. The pressure data for the different sea states show very similar qualitative and quantitative results, compared to the FSE data. The deviation for all PGs in the different sea states lies in the range of 5% $\leq$NRMSE$\leq$ 10%.

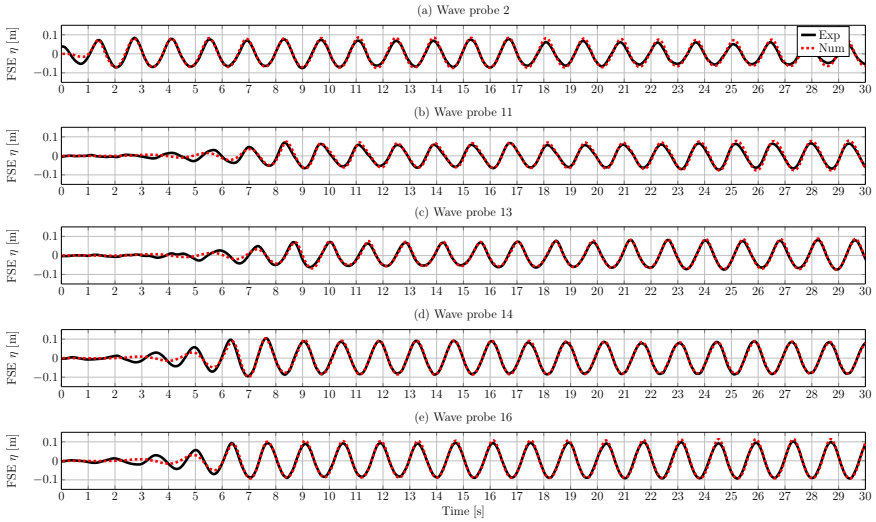

Figure 14: Experimental and numerical FSE data for sea state MS02

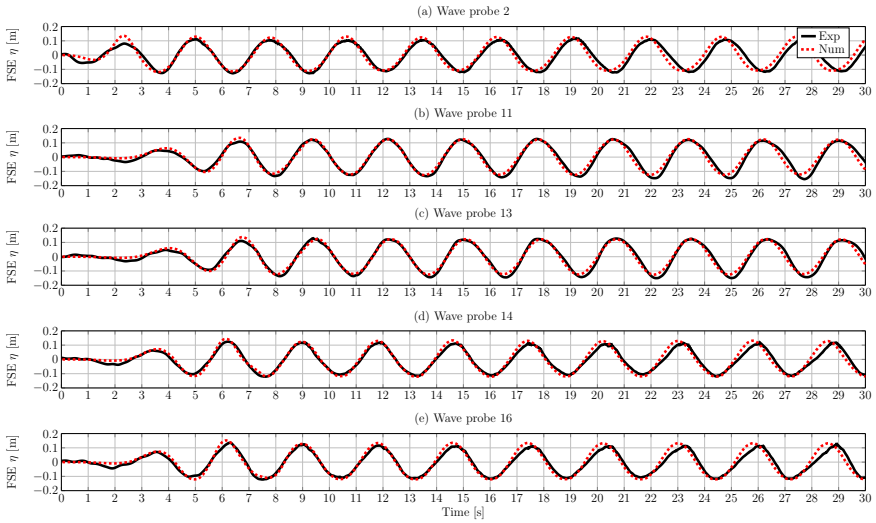

Figure 15: Experimental and numerical FSE data for sea state MS04

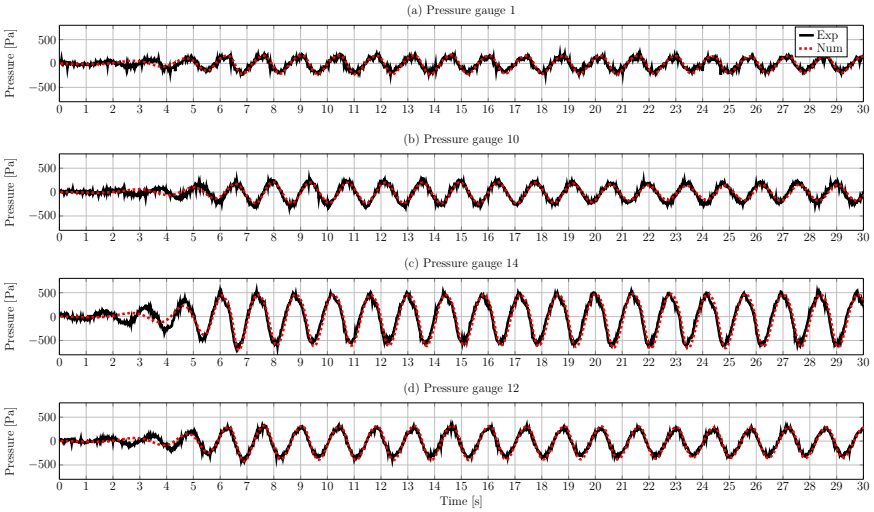

Figure 16: Experimental and numerical pressure data for sea state MS02

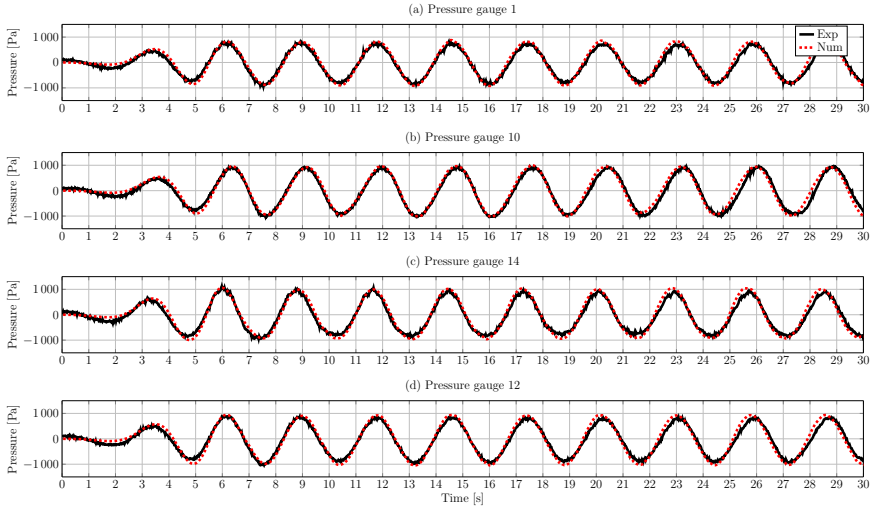

Figure 17: Experimental and numerical pressure data for sea state MS04

Table 10: Normalised RMSE between numerical and experimental FSE and pressure data for diffraction test cases

FSE					
WP #	2	11	13	14	16
MS01 [m]	–	–	–	–	–
MS02 [m]	0.07	0.07	0.05	0.05	0.05
MS03 [m]	–	–	–	–	–
MS04 [m]	0.11	0.07	0.06	0.08	0.09
Pressure					
PG #	1	10	14	12	
MS01 [Pa]	0.08	0.09	0.05	0.07	
MS02 [Pa]	0.10	0.08	0.09	0.07	
MS03 [Pa]	0.10	0.10	0.06	0.09	
MS04 [Pa]	0.08	0.09	0.08	0.09	

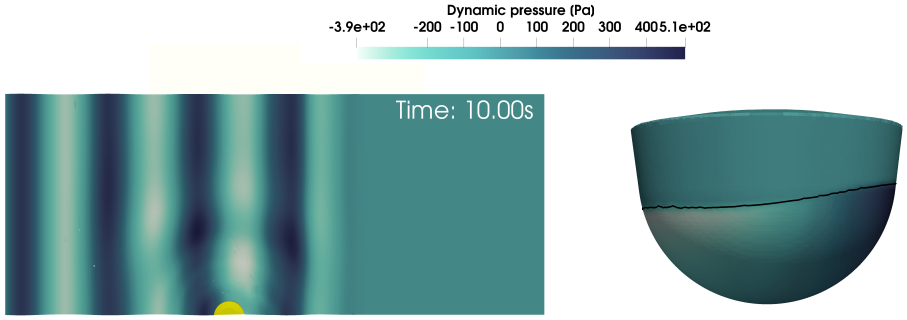

Figure 18: Screen shots of the dynamic pressure field across the domain (left), and on the WEC body (right) for sea state MS02. The black line on the WEC hull indicates the instantaneous free surface.

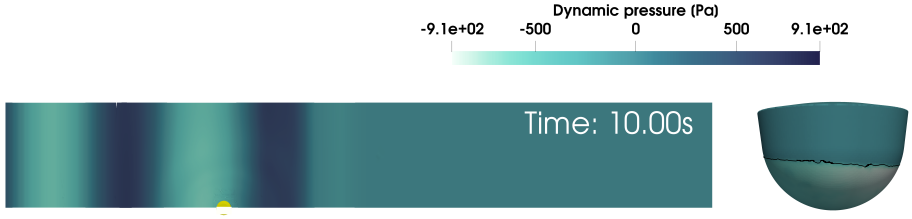

Figure 19: Screen shots of the dynamic pressure field across the domain (left), and on the WEC body (right) for sea state MS04. The black line on the WEC hull indicates the instantaneous free surface.

5.3. Wave Radiation

The wave radiation tests provide a first validation of the WEC response to the PTO force, analysing the PTO cylinder displacement and the pressure on the WEC hull (at PGs 1, 10, 14 and 12). The FSE data are omitted from the compaison, due to the high signal-to-noise ratio in the experimental data. The time series of the PTO force measured at the 1 DoF load cell in the experiments is used as the input for the CNWT experiments.

5.3.1. Analysis

The NRMSE values for the cylinder displacement and the pressure data are listed in Table 11. Figures 20a to 20c show time traces for the cylinder displacement for the DA300F35, DA400F35 and DA600F35 cases, respectively. Pressure data from the PGs are plotted in Figure 21 for the test case DA300F35. By way of example, Figure 22 shows the dynamic pressure distribution over the WEC hull at three time instances, for case DA300F35.

From the qualitative comparison of the cylinder displacement in Figure 20a, a sufficient agreement between the numerical and experimental data set can be observed. The phase of the signals matches very well, while some over- and under-prediction of the peak and trough values is found, respectively. This is also reflected in the NRMSE in Table 11. The validation of the pressure data is also good (NRMSE$<$ 8%) and the trend in NRMSE for the three cases correlating with the results from the cylinder displacement data, with DA400F35 having the smallest NRMSE and DA300F35 the largest. This is expected since, for wave radiation tests, the pressure is directly related to the body motion.

(a) DA300F35

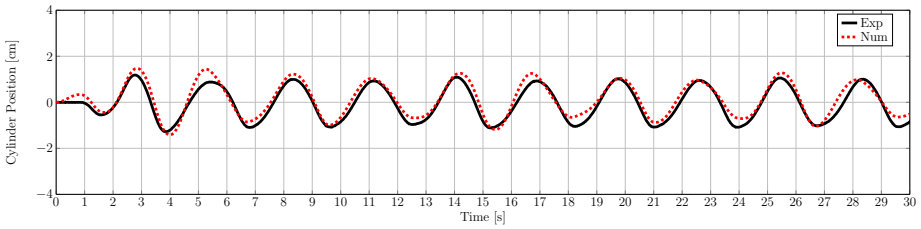

(b) DA400F35

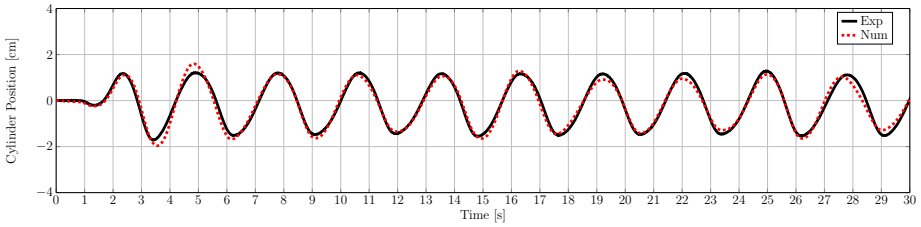

(c) DA600F35

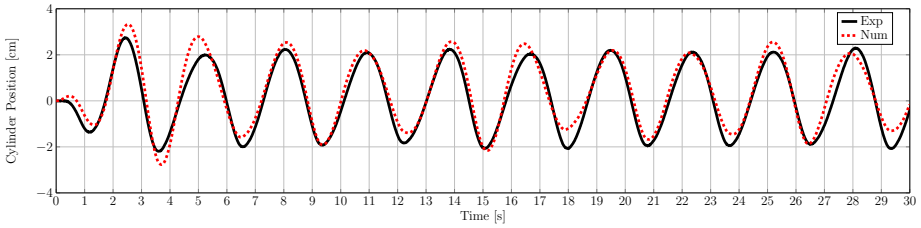

Figure 20: Numerical and experimental cylinder position force for radiation tests

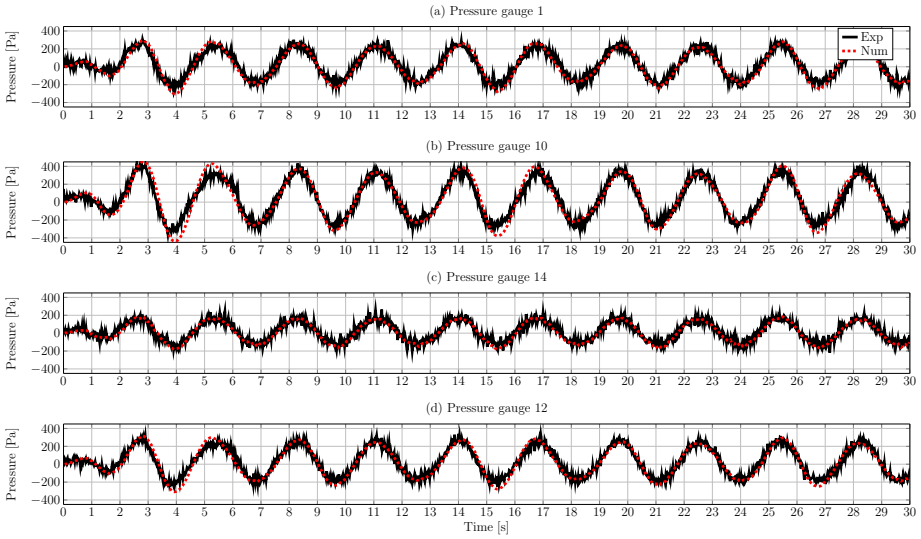

Figure 21: Experimental and numerical pressure data for radiation test case DA300F35

Table 11: Normalised RMSE between numerical and experimental cylinder position and pressure data for radiation test cases

	Cylinder Displ.	**Pressure**			
	Xc	PG1	PG10	PG14	PG12
DA300F35	0.10	0.07	0.07	0.07	0.07
DA400F35	0.05	0.05	0.06	0.06	0.06
DA600F35	0.09	0.07	0.08	0.06	0.08

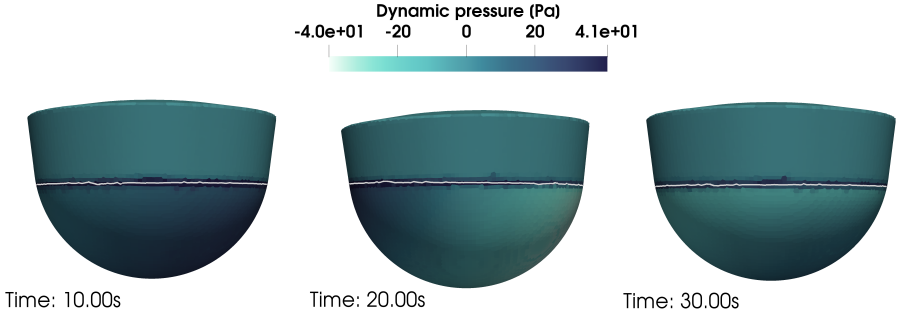

Figure 22: Screen shots of the dynamic pressure field on the WEC hull for radiation test case DA300F35. The grey line on the WEC hull indicates the instantaneous free surface. The time instances represent maximum cylinder etraction (10s & 30s), and maximum cylinder extension (20s).

5.4. WEC with PTO system

The *full* WSI, with WEC motion driven by waves and PTO forces, is finally considered for validation in this test case. Comparison is made between experimental and numerical results for the PTO cylinder displacement and velocity, PTO force (at the 1 DoF load cell), generated power, FSE at WPs 2, 11 and 14, and the pressure on the WEC hull at PGs 1, 10, 14 and 12.

As in the previous sections, the quantitative comparison is achieved using the NRMSE, and qualitative comparison is achieved through the inspection of plotted time traces. For clarity, this section is divided into subsections according to the considered sea state, plus an initial subsection describing the calibration of the PTO model.

5.4.1. PTO model

Before the CNWT simulations can be performed, the user-defined spring stiffness, K_{num}, and damping, D_{num}, coefficients of the linear spring-damper PTO system in the CNWT must be calibrated to represent its physical equivalent. Since resistive control is employed in the physical WEC model, only damping and no reactive force, i.e. $K_{num} = 0$, should be applied by the PTO (see Equation (1)). However, calculating an equivalent linear damping coefficient, using Equation (1) and geometrical transformation, did not lead to expected results from the CNWT simulations, when validated against the PWT data.

Inspection of the zero damping case, $D_{exp} = 0$, revealed that a PTO force was still being applied. Further inspection revealed that the time average of the power flow to the WEC from the PTO force was non-zero, meaning that the PTO was applying reactive power i.e. $K_{num} \neq 0$. This *residual* reactive power may stem from delays of the controller and hardware between target and actual force, in the physical tank.

Furthermore, it is well known, that any PWT setup experiences friction in the mechanical parts. This friction, generally, is a non-measurable quantity, which makes its replication in the numerical setup a challenging task.

To correctly replicated the PWT setup in the CNWT, calibration of the PTO coefficients D_{num} and K_{num} is required. Here, a linear least squares approach is employed on the PWT data, assuming that the PTO force follows the simple relation shown in Equation (9). F_{PTO}, $x_{PTO}(t)$ and $v_{PTO}(t)$ are the measured PTO force, cylinder displacement and velocity in the PWT experiments, respectively.

A least square regression, as shown in Equations (11)–(13), can be constructed, where ξ_j contains the damping and stiffness coefficients, while $\varphi_j(t)$ contains velocity and position data.

$$F_{PTO}(t, \xi) = \sum_{j=1}^{2} \xi_j \varphi_j(t) \tag{11}$$

$$X_{ij} = \varphi_j(t_i) \tag{12}$$

$$\hat{\xi} = \left(X^T X\right)^{-1} X^T F_{PTO} \tag{13}$$

The resulting estimated K_{num} and D_{num} values from the least squares fit for the different D_{exp} values, for sea states MS01-MS03, are plotted in Figure 23, showing consistent estimates for K_{num} and D_{num} between the different sea states. Additionally, a clear linear trend in the increase of K_{num} and D_{num} with the increase of D_{exp} can be seen. Linear regression is used again to create a line of best fit through the K_{num} and D_{num} values (also plotted in Figure 23), yielding the following relationships:

$$K_{num} = 184 D_{exp} - 4700 \tag{14}$$

$$D_{num} = 70 D_{exp} \tag{15}$$

Equations (14) and (15) are used to calculate the user-defined linear spring-damper coefficients for the CNWT simulations, which are listed in Table 12. It should be noted that the values in Table 12 are 50% of those shown in Figure 23, to account for the symmetry plane used in the CNWT.

It should further be noted that the necessary integration of a non-zero spring stiffness highlights the importance of PTO dynamics. Real hydraulic systems may have their own spring and/or inertia effects that can lead to effective provision of reactive power. Therefore, it is important to adequately define these using available data, or implement a high-fidelity PTO system as shown in [5].

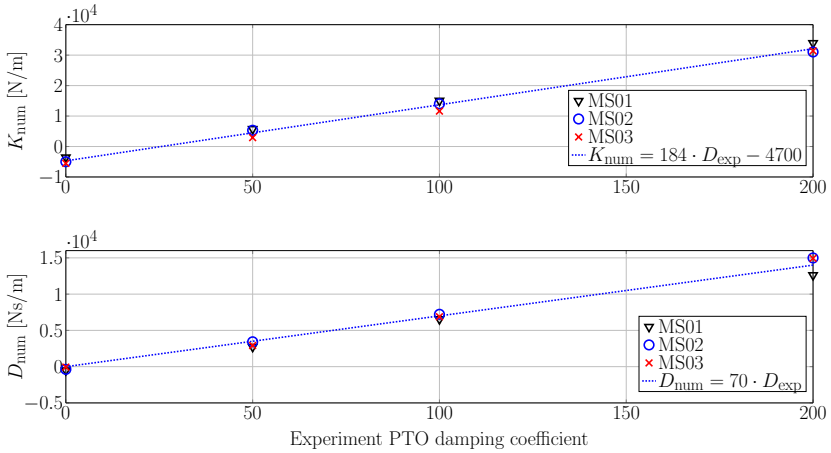

Figure 23: Spring stiffness and damping coefficient determine through linear least squares regression

Table 12: Spring stiffness and damping coefficient determine through linear least squares regression

D_{exp} [N m s]	D_{num} [N s m^{-1}]	K_{num} [N m^{-1}]
0	0	-23502
50	1750	2250
100	3500	6850
200	7000	16050

5.4.2. Analysis: MS01

For the case of highest experimental damping, $D_{exp} = 200$N m s, the NRMSE for the PTO data (position, velocity, force) and instantaneous, generated power as well as the pressure data and FSE are listed in Table 13, and the time traces for the PTO, pressure and FSE are plotted in Figures 24 to 26, respectively. From the PTO data, good agreement can be observed, with NRMSEs of $< 10\%$ for the position and velocity and 12% for the PTO force. The magnitude for position, velocity and force is over-predicted, while phase is captured well. The experimental force signal shows second order effects in the troughs, which are not captured in the numerical model. However, due to the small force amplitude, it is not clear if these effects stem from noise in the recorded data, or reflect actual PTO characteristics.

The instantaneous, generated power is calculated as the product between the instantaneous PTO force and velocity. For the case of $D_{exp} = 200$N m s, an NRMSE of 25% is calculated. The error in the power is larger compared to the NRMSE for the velocity and force, because error accumulation from the velocity and force signals appears.

Inspection of the pressure time series, plotted in Figure 25, also reveals good agreement. The largest NRMSE, 13%, is found at PG1 and can be attributed to the low SNR in the experimental data. The smallest NRMSE, 6%, occurs at PG14 which faces the wave generator. For PG10 (NRMSE=13%) and PG12 (NRMSE= 10%) a small phase lag results in a larger NRMSE.

The FSE time series at WP2, WP11 and WP14 are plotted in Figure 26, and NRMSE values are listed in Table 13. Again, good qualitative and quantitative (NRMSE$\leq$ 12%) agreement is found. The deviation in FSE is found to be larger than for the wave-only cases (NRMSE$\leq$ 2%), which could be attributed to the interaction between radiated and diffracted waves. The largest deviation can be found at WP11, in the wake of the body, where a phase lag causes the mismatch. This lag coincides with the phase lag of PG10 which is also located at the downwave side of the hull.

In a similar fashion, results for the cases $D_{exp} = 100, 50$ and 0 N m s are analysed. PTO data are plotted in Figures 27 to 29, while pressure data are plotted in Figures 30 to 32, respectively. Since FSE data show consistent behaviour for all different damping values, these plots are omitted for brevity. Screen shots of the velocity vectors are shown in Figures 33 (a)–(d) for all the different PTO

damping values. Furthermore, Figures 34 (a)–(d) show the wave field in the CNWT at a specific time instance and the distribution of the dynamic pressure on the hull. These screen shots highlight the similarity of the FSE for all different damping values. Furthermore, Table 13 contains the NRMSE for all data.

For a PTO damping of $D_{exp} = 100\,\mathrm{N\,m\,s}$ good quantitative and qualitative agreement for PTO Data (NRMSE$\leq$ 7%), generated power (NRMSE=8%), FSE (NRMSE$\leq$ 8%) and pressure (NRMSE$\leq$ 14%) can be found. Specifically the PTO position and velocity is captured well, with a NRMSE of 5%. Error accumulation can be observed for the generated power, resulting in a relatively large error, compared to the PTO velocity and force. The pressure signals show similar behaviour to the $D_{exp} = 200\,\mathrm{N\,m\,s}$ case.

For $D_{exp} = 50\,\mathrm{N\,m\,s}$, the position and velocity data show similar agreement to the $D_{exp} = 200\,\mathrm{N\,m\,s}$ case (NRMSE=6%). The plotted time traces show an under-estimation of the motion amplitudes in the numerical simulation. The force magnitude is captured well, resulting in a NRMSE of 9%. Good agreement in phase can be observed for all PTO data. For the generated power a NRMSE of 10% can be found. The pressure signals for $D_{exp} = 50\,\mathrm{N\,m\,s}$ show a fit comparable the previous cases (NRMSE$\leq$ 13%), with the same deviation characteristics.

For the case of $D_{exp} = 0\,\mathrm{N\,m\,s}$, the agreement between experimental and numerical PTO and pressure data decreases significantly (NRMSE$\leq$ 48%). Overall, the PTO position and velocity is under-predicted in the numerical model, resulting in a NRMSE of 11% (see Figure 29). The PTO force shows the most severe deviation. While the force amplitude is captured reasonably well, an almost 180° phase lag can be observed. However, since the force amplitude is very small (approx. $\pm$200N), other background dynamics in the PTO system (or possibly gantry vibrations), with a high frequency oscillation, cause a non-negligible force, corrupting the signal and making the comparison difficult. The large error in the PTO force influences the accuracy of the instantaneous, gerated power, resulting in a NRMSE of 38%. The mismatch in body motion is also reflected in the measured pressure at PG1 (NRMSE=12%), 10 (NRMSE=11%) and 12 (NRMSE=13%) (see Figure 32). At these probes, a similar pattern, as in the position/velocity data, can be observed. Interestingly, the pressure data at PG14 (NRMSE=15%), facing the wave generator, seems less affected by the previously described mismatch in motion amplitude, and show good agreement for the pressure magnitude. However, a phase lag causes the relatively large NRMSE.

Although the numerical zero-damping case shows significant deviations compared to the experimental data, with the confidence given through the good agreement of larger PTO damping cases, the hydrodynamic model of the device is effectively validated for sea state MS01.

Table 13: NRMSE between numerical and experimental PTO data for sea state MS01

D_{exp}[N m s]	200	100	50	0
PTO Data				
Position	0.08	0.05	0.06	0.11
Velocity	0.08	0.05	0.06	0.11
Force	0.12	0.07	0.09	0.44
Power	0.25	0.08	0.10	0.38
Pressure				
PG 1	0.13	0.07	0.08	0.12
PG 10	0.13	0.09	0.11	0.11
PG 14	0.06	0.10	0.08	0.15
PG 12	0.10	0.14	0.13	0.13
FSE				
WP 2	0.08	0.07	0.07	0.06
WP 11	0.12	0.08	0.09	0.07
WP 14	0.06	0.07	0.10	0.12

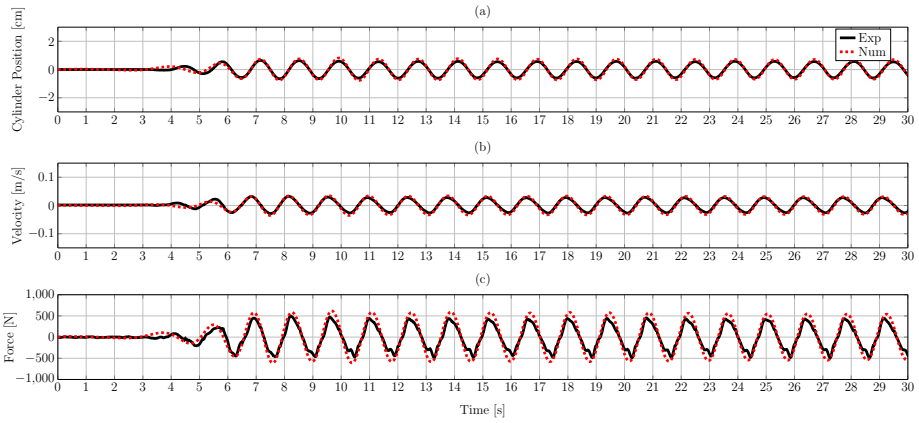

Figure 24: Numerical and experimental PTO data for sea state MS01 with experimental damping $D_{exp} = 200$N m s

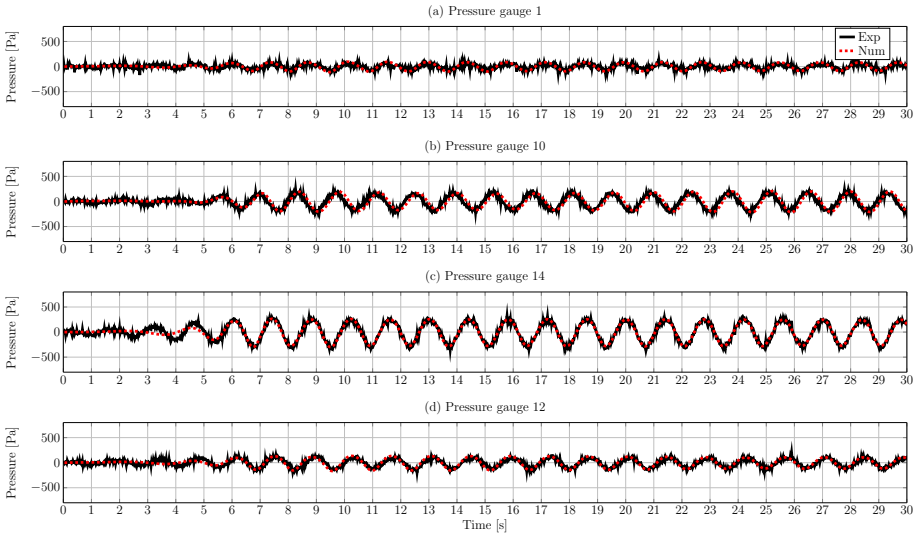

Figure 25: Numerical and experimental pressure data for sea state MS01 with experimental damping $D_{exp} = 200\text{N m s}$

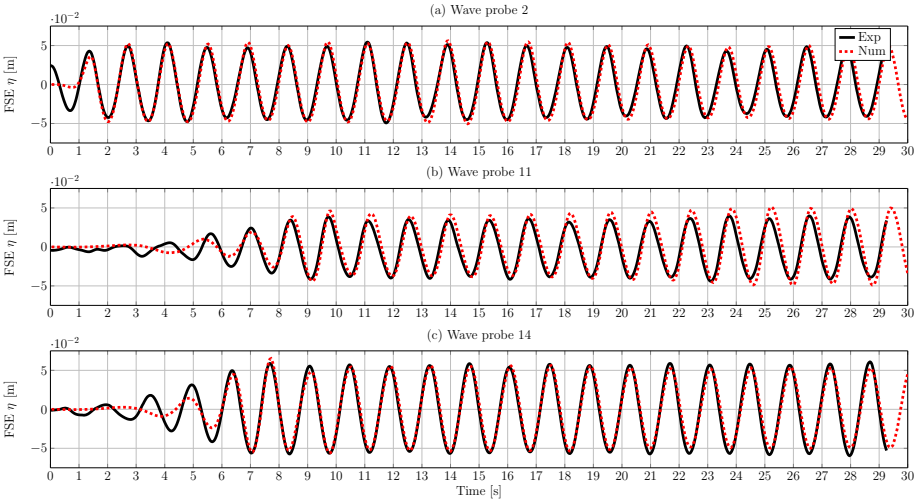

Figure 26: Numerical and experimental FSE data for sea state MS01 with experimental damping $D_{exp} = 200\text{N m s}$

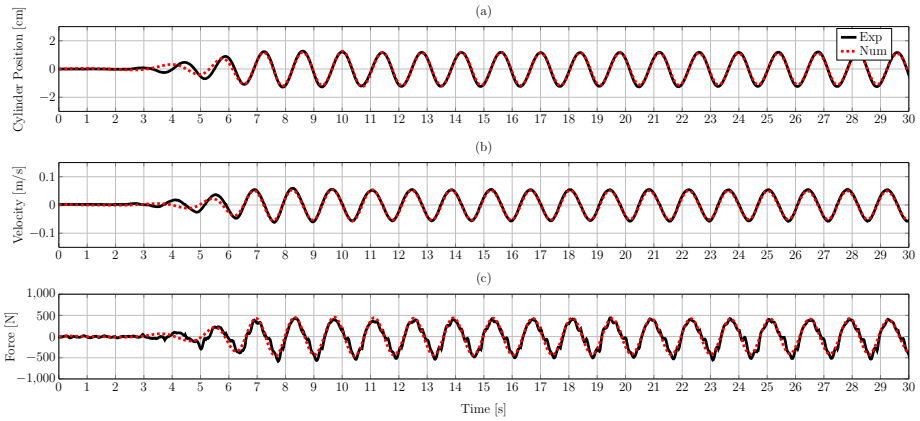

Figure 27: Numerical and experimental PTO data for sea state MS01 with experimental damping $D_{exp} = 100\text{N m s}$

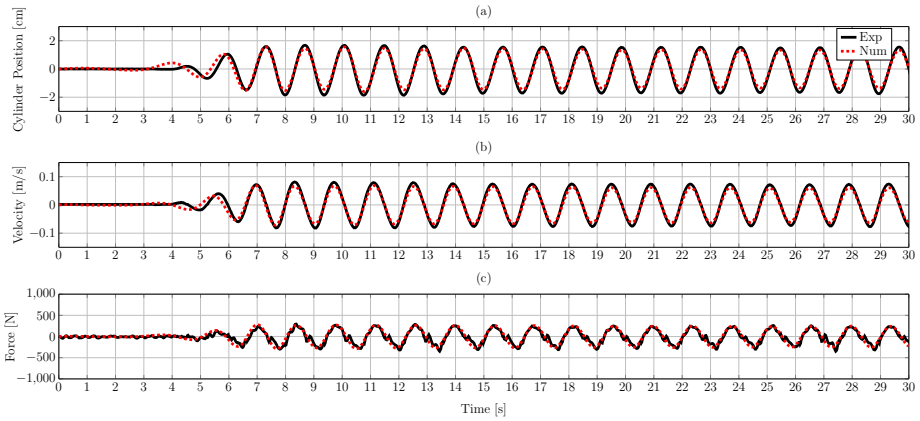

Figure 28: Numerical and experimental PTO data for sea state MS01 with experimental damping $D_{exp} = 50\text{N m s}$

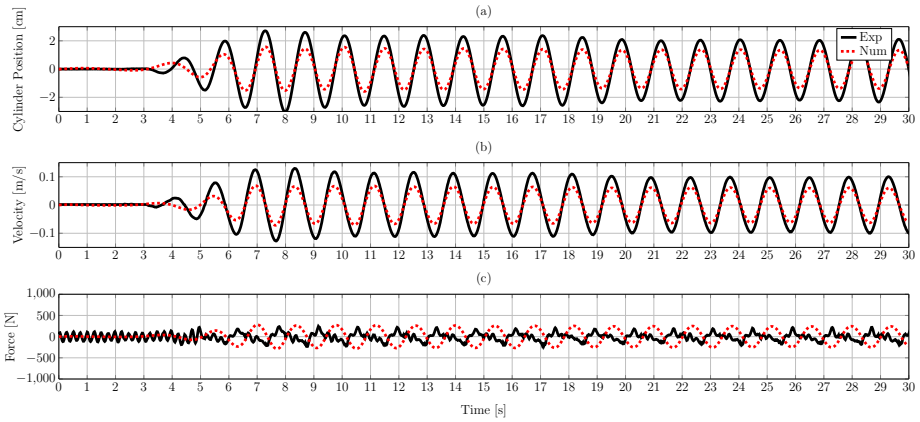

Figure 29: Numerical and experimental PTO data for sea state MS01 with experimental damping $D_{exp} = 0\,\mathrm{N\,m\,s}$

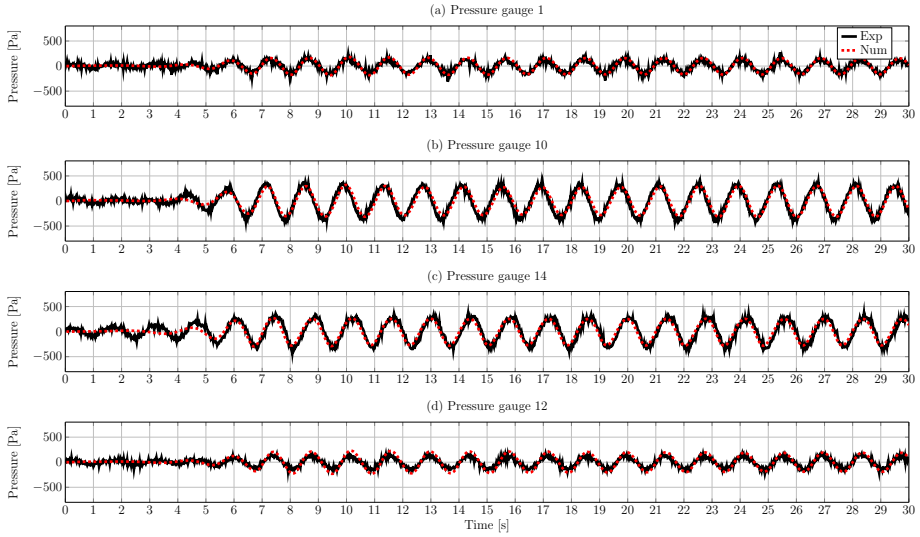

Figure 30: Numerical and experimental pressure data for sea state MS01 with experimental damping $D_{exp} = 100\,\mathrm{N\,m\,s}$

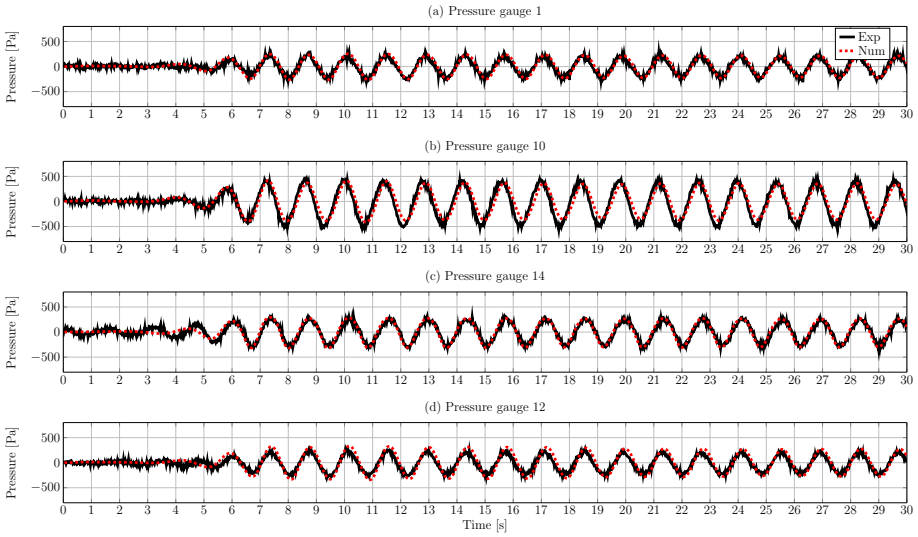

Figure 31: Numerical and experimental pressure data for sea state MS01 with experimental damping $D_{exp} = 50\text{N m s}$

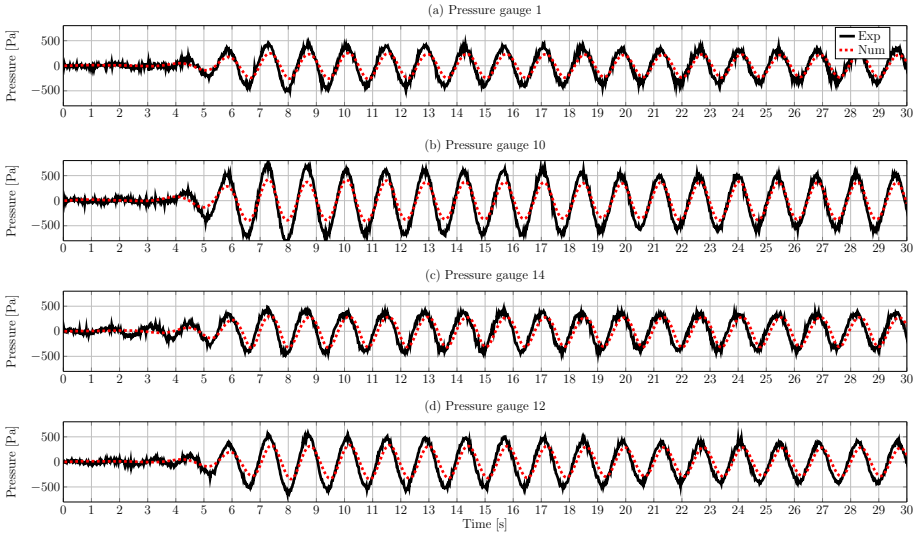

Figure 32: Numerical and experimental pressure data for sea state MS01 with experimental damping $D_{exp} = 0\text{N m s}$

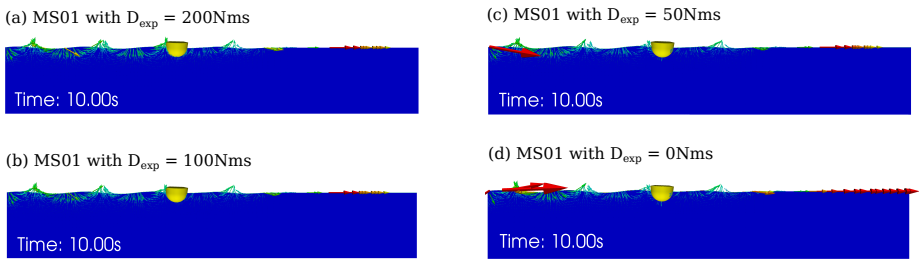

Figure 33: Screen shots of the computational domain showing the α_{VF} field, and the normalised velocity vectors.

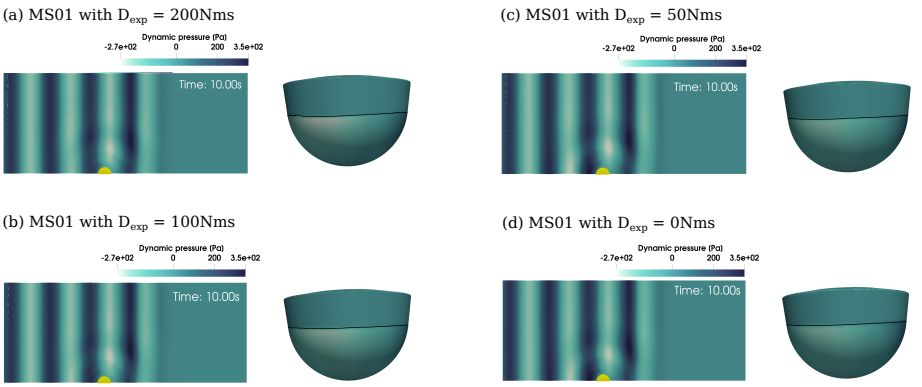

Figure 34: Screen shots of the dynamic pressure field across the domain (left), and on the WEC hull (right), for sea state MS01. The black line on the WEC hull indicates the instantaneous free surface.

5.4.3. Analysis: MS02

In this test case, the wave height is increased from 0.1m to 0.15m, compared to MS01. The NRMSE for the PTO signals (position, velocity, force), instantaneous, generated power, pressure and FSE data are listed in Table 14. For brevity, time traces of the PTO data and pressure are only plotted for cases $D_{exp} = 200\,\mathrm{N\,m\,s}$ and $D_{exp} = 0\,\mathrm{N\,m\,s}$ (see Figures 35 to 38). Since the FSE data show consistently good agreement with NRMSE$\leq$ 11%, for brevity, plots are omitted.

Starting again with the highest damping, $D_{exp} = 200\,\mathrm{N\,m\,s}$, the PTO data show good agreement, with a maximum NRMSE of 10%, for position, velocity and force. Excellent agreement in phase is achieved, while the amplitudes for position (NRMSE=10%) and velocity (NRMSE=9%) are over-predicted. For the PTO force, taking into account the noise in the experimental data, the amplitude is well captured in the numerical model (NRMSE=9%). For the instantaneous, generated power, a relatively large NRMSE of 21% can be found. This large error is the result of the over-prediction of the numerical PTO velocity and the noise seen in the experimental data. Inspection of the pressure time series, plotted in Figure 36, supports the good fit of the PTO position, velocity and force. Particularly at PG14, good agreement, with a NRMSE of 6% is achieved. The larger deviation at PG1 (NRMSE=12%) can be attributed to the high noise level in the experimental data. For PG10 (NRMSE=19%) a phase lag causes the large NRMSE. At PG12 (NRMSE= 11%), again, satisfying results can be observed. For the FSE data, good qualitative and quantitative (NRMSE$\leq$ 10%) agreement is found. The deviation in FSE is again found to be larger than for the waves-only cases (NRMSE$\leq$ 2%), which could be attributed to the influence of the radiated and diffracted waves by the WEC, which is highlighted by the good match farthest away form the device (WP2) and increased deviations in vicinity to the body (WP11 and WP14).

For a PTO damping of $D_{exp} = 100\,\mathrm{N\,m\,s}$ similarly good quantitative and qualitative agreement for PTO position (NRMSE=8%), velocity (NRMSE=7%) and force (NRMSE=8%) can be found. Error accumulation can be observed for the generated power, resulting in a relatively large error (NRMSE=15%), compared to the PTO velocity and force. Larger deviation can be observed for the pressure measured at PG1 (NRMSE=18%), PG10 (NRMSE=23%) and PG12 (NRMSE=22%). At PG1, an over-prediction of the pressure leads to the increased NRMSE. However, given the SNR, the deviations lie within an acceptable range. At PG10, the phase lag between experimental and numerical results leads to increased quantitative deviation. The magnitude, however, compares well. At PG12 an over-prediction of the pressure leads to the increased NRMSE. The phase is captured reasonably well.

For $D_{exp} = 50\,\mathrm{N\,m\,s}$, best agreement can be observed for the PTO data, with minimum NRMSE of 6%, and generated power, , with a NRMSE of 9%. For the pressures, similarly larg deviations as for $D_{exp} = 100\,\mathrm{N\,m\,s}$ occur at PG1 (NRMSE=17%), PG10 (NRMSE=21%) and PG12 (NRMSE=19%). These stem from a phase lag, while pressure magnitudes compare well for all pressure

probes.

For the case of $D_{exp} = 0\,\mathrm{N\,m\,s}$, the agreement between experimental and numerical PTO and pressure data decreases. Overall, the PTO position (NRMSE=9%) and velocity (NRMSE=8%) is under-predicted in the numerical model (see Figure 37). Furthermore, the body motion does not reach a steady state. Since the zero damping case is associated with the most significant WEC motion, it might be assumed that larger radiated waves are being produced and reflecting off the non-absorbing side walls, which influences the body motion. The deviation in body motion is also reflected in the measured pressure at PG1 (NRMSE=10%), PG10 (NRMSE=11%) and PG12 (NRMSE=10%) (see Figure 38). At these probes, a similar pattern, as in the position/velocity data, can be observed. Interestingly, the pressure data at PG14, facing the wave generator, seems unaffected by the described mismatch in body motion, and still shows good agreement with experimental data. This suggests that the incoming wave is unaffected (i.e. no non-linear interaction) by the wave radiation from the body and reflections mostly coming from the tank side walls. Lastly, comparing the PTO force, it can be stated that the force amplitude and phase in the numerical model and the experimental show good agreement. However, the low SNR in the experimental data, leads to a relatively large NRMSE of 14%, and subsequently to a NRMSE of 13% for the generated power. Compared to sea state MS01, the use of a negative spring stiffness in the numerical model is able to reasonably replicate the experimental system dynamics, for the case of zero damping. This may be reasoned with the larger oscillation amplitude, mitigating unrepresented effects of the other background dynamics in the PTO and other system components.

Table 14: NRMSE between numerical and experimental PTO data for sea state MS02

D_{exp}[N m s]	200	100	50	0
PTO Data				
Position	0.10	0.08	0.06	0.09
Velocity	0.09	0.07	0.06	0.08
Force	0.09	0.08	0.07	0.14
Power	0.21	0.15	0.09	0.13
Pressure				
PG 1	0.12	0.18	0.17	0.10
PG 10	0.19	0.23	0.21	0.11
PG 14	0.06	0.07	0.10	0.08
PG 12	0.11	0.22	0.19	0.10
FSE η				
WP 2	0.06	0.06	0.08	0.07
WP 11	0.06	0.07	0.10	0.09
WP 14	0.10	0.09	0.07	0.10

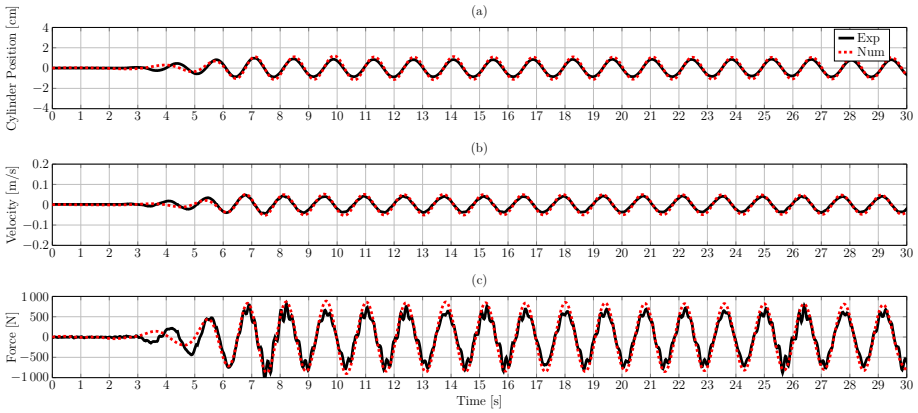

Figure 35: Numerical and experimental PTO data for sea state MS02 with experimental damping $D_{exp} = 200\text{N m s}$

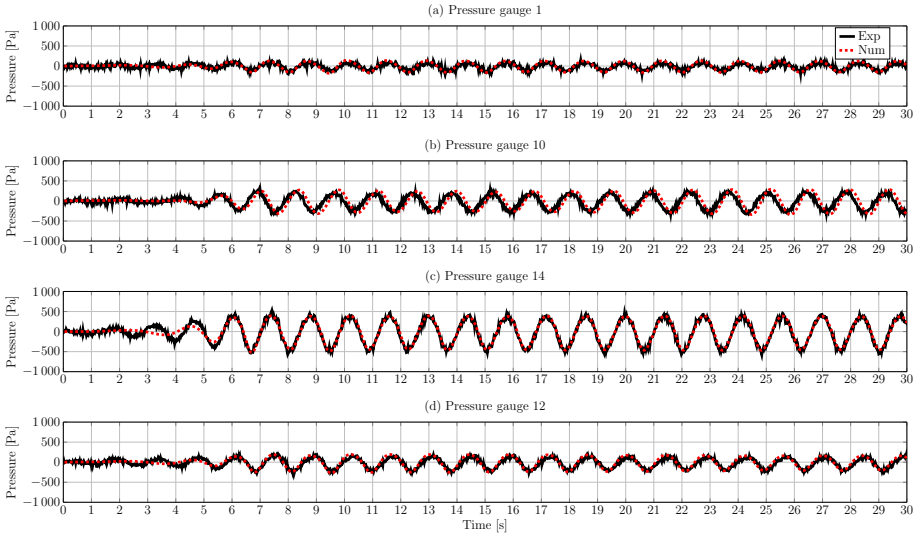

Figure 36: Numerical and experimental pressure data for sea state MS02 with experimental damping $D_{exp} = 200\text{N m s}$

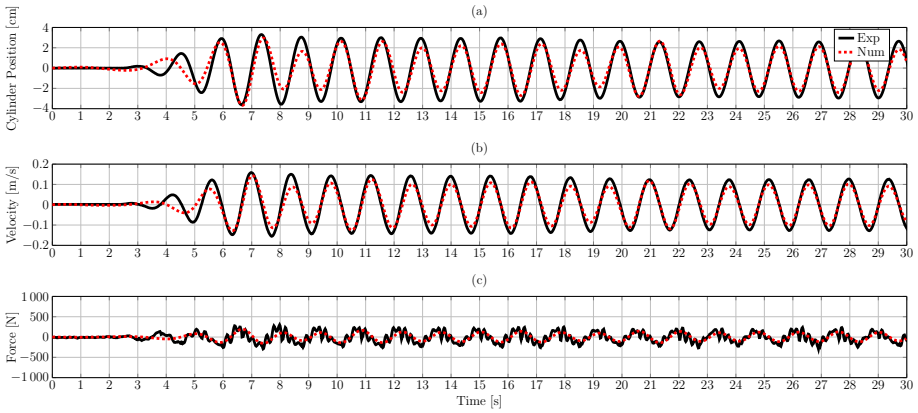

Figure 37: Numerical and experimental PTO data for sea state MS02 with experimental damping $D_{exp} = 0\,\mathrm{N\,m\,s}$

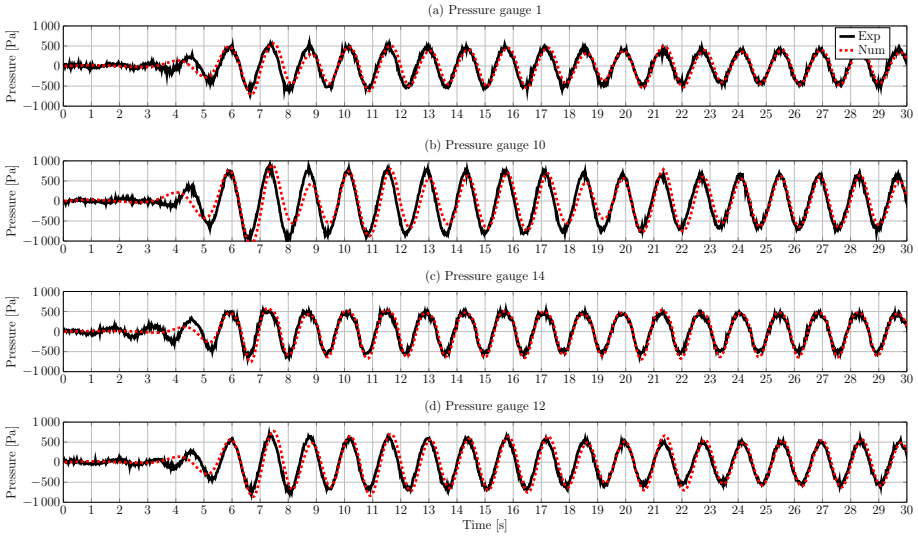

Figure 38: Numerical and experimental pressure data for sea state MS02 with experimental damping $D_{exp} = 0\,\mathrm{N\,m\,s}$

5.4.4. Analysis: MS03

Considering an even larger wave height, i.e. 0.25m, the agreement between experimental and numerical results for the different PTO damping settings show comparable accuracy, compared to the previous sea states. The quantitative comparisons are listed in Table 15 and the qualitative plots in Figures 39 to 42.

From the quantitative and qualitative comparison of the FSE data for all damping values, a mismatch in the wave period becomes obvious, leading to divergence of the phase after approx. 19s simulated time (see Figure 41). Note, for brevity, FSE data are only plotted for the single case of $D_{exp} = 200\,\mathrm{N\,m\,s}$. This phase divergence in the FSE consequently leads to a mismatch in phase for the PTO and pressure data, resulting in relatively large NRMSE values, up to 13% for the PTO force, 18% for the instantaneous, generated power and 26% for the pressure. Furthermore, for all cases, an increasing mismatch in wave amplitude in vicinity of the body (i.e. WP11 and WP14), specifically an under-prediction, can be observed (see Figure 41). This however, is not reflected in the PTO and pressure data (for cases $D_{exp} = 200 - 50\,\mathrm{N\,m\,s}$), where good agreement in the position, velocity, force and pressure magnitudes is achieved. Only PG12 shows consistently poor agreement due to an over-prediction of the pressure amplitude.

For $D_{exp} = 0$, the results show very similar behaviour, as for MS02. Again, an overall under-prediction of position, velocity and force can be seen in the numerical model. Also, no steady state is reached. For the pressure, the fluctuation is reflected at PG1, PG10 and PG12, while, again, a good fit at PG14 is achieved. Here, the experimental data show a characteristic plateau at the pressure peaks. This is very well captured in the numerical model.

Table 15: NRMSE between numerical and experimental PTO data for sea state MS03

D_{exp}[N m s]	200	100	50	0
PTO Data				
Position	0.10	0.11	0.12	0.12
Velocity	0.10	0.11	0.11	0.12
Force	0.10	0.11	0.12	0.13
Power	0.18	0.18	0.18	0.15
Pressure				
PG 1	0.14	0.16	0.14	0.09
PG 10	0.14	0.11	0.17	0.09
PG 14	0.08	0.11	0.10	0.08
PG 12	0.17	0.26	0.21	0.08
FSE				
WP 2	0.14	0.14	0.16	0.18
WP 11	0.10	0.12	0.09	0.13
WP 14	0.21	0.22	0.18	0.18

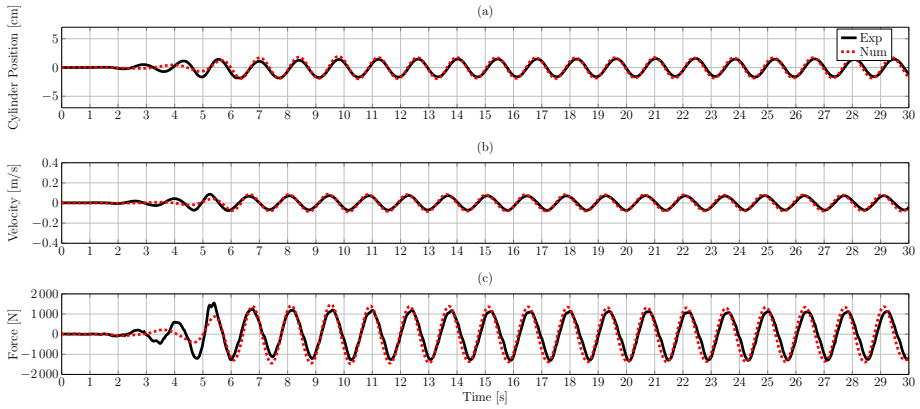

Figure 39: Numerical and experimental PTO data for sea state MS03 with experimental damping $D_{exp} = 200\text{N m s}$

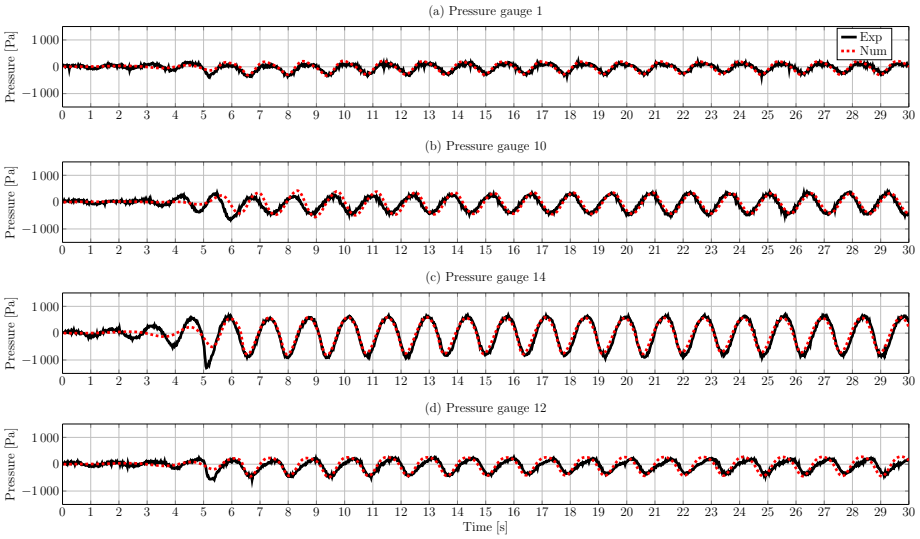

Figure 40: Numerical and experimental pressure data for sea state MS03 with experimental damping $D_{exp} = 200\text{N m s}$

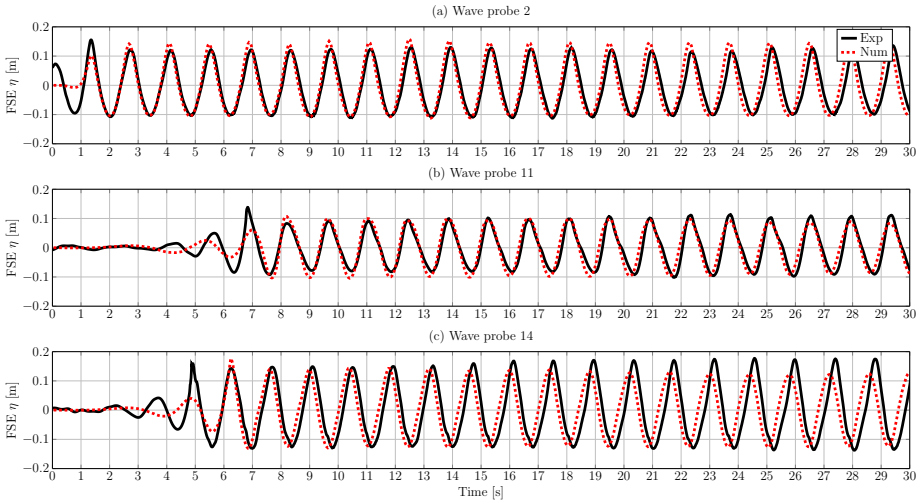

Figure 41: Numerical and experimental FSE data for sea state MS03 with experimental damping $D_{exp} = 200\text{N m s}$

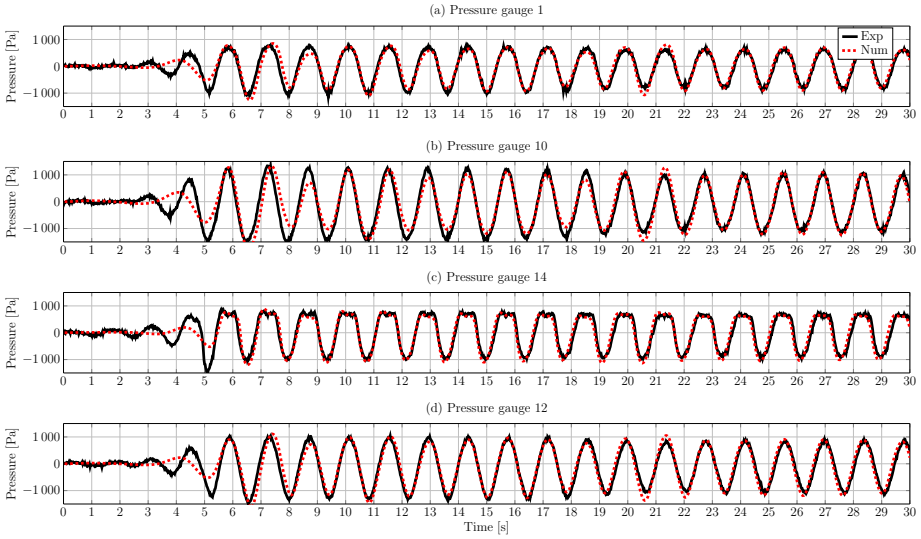

Figure 42: Numerical and experimental pressure data for sea state MS03 with experimental damping $D_{exp} = 0\text{N m s}$

5.4.5. Analysis: MS04

As a final sea state, MS04 is considered for validation. While, for the previous test cases, the wave period is constant at 1.4s, the wave period for MS04 is 2.8s. The availability of experimental data for MS04 only allows for the comparison at a single PTO damping setting, i.e. $D_{exp} = 200\,\mathrm{N\,m\,s}$, which, based on the least squares regression from sea states MS01-MS03, results in a numerical damping coefficient and spring stiffness of $D_{num} = 7000\,\mathrm{N\,s\,m^{-1}}$ and $K_{num} = 16050\,\mathrm{N\,m^{-1}}$, respectively. Quantitative results are listed in Table 16. For a qualitative comparison, PTO data are plotted in Figure 43–45.

Overall, similar results, as in the previous test cases, are found. For the surface elevation, all NRMSE values fall below 13%, which is expected with respect to the results found for the waves-only case in Section 5.1. The PTO cylinder displacement and velocity show relatively small deviations with NRMSEs of 6%. The force signal reveals a relatively small over-prediction of the PTO force in the numerical model. Furthermore, a phase lag in the experimental force signal can be observed, leading to a NRMSE of 18%, which is reflected in the NRMSE of the instantaneous, generated power of 19%. This suggests that the employed combination of spring stiffness and damping coefficient does not accurately represent the physical system, which, in turn, suggests that the estimated coefficients D_{num} and K_{num}, to replicate the physical PTO system, are frequency dependent, implying non-linearity of the physical PTO system.

The phase deviation, found in the PTO force signal, also appears in the pressure data at all PGs. Both force and pressure show a phase lag of approx. 0.3s. This highlights the assumption that the characteristics of the physical system are frequency dependent and currently not accurately represented in the numerical model. However, for the purpose of this study, the agreement between numerical and experimental results is satisfying.

Table 16: NRMSE between numerical and experimental PTO data for sea state MS04

	$D_{exp} = 200\mathrm{N\,m\,s}$
PTO Data	
Cylinder Position	0.06
Cylinder Velocity	0.06
Cylinder Force	0.18
Power	0.19
Pressure	
Pressure gauge 1	0.18
Pressure gauge 10	0.27
Pressure gauge 14	0.18
Pressure gauge 12	0.19
FSE η	
Wave probe 2	0.13
Wave probe 11	0.09
Wave probe 14	0.12

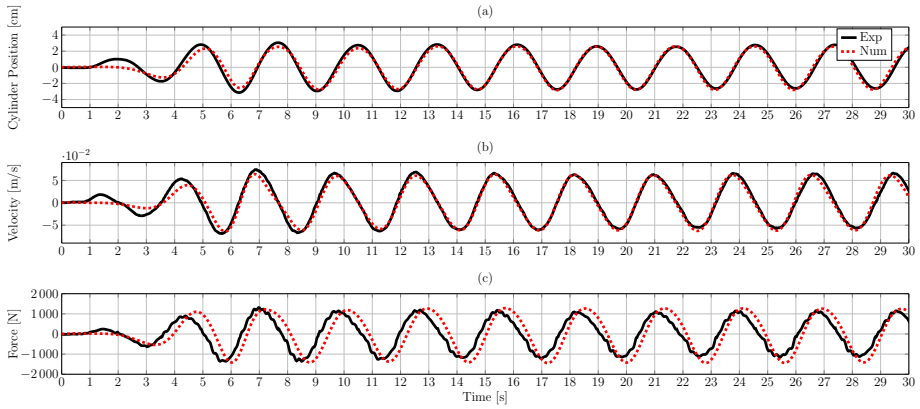

Figure 43: Numerical and experimental PTO data for sea state MS04 with experimental damping $D_{exp} = 200\text{N m s}$

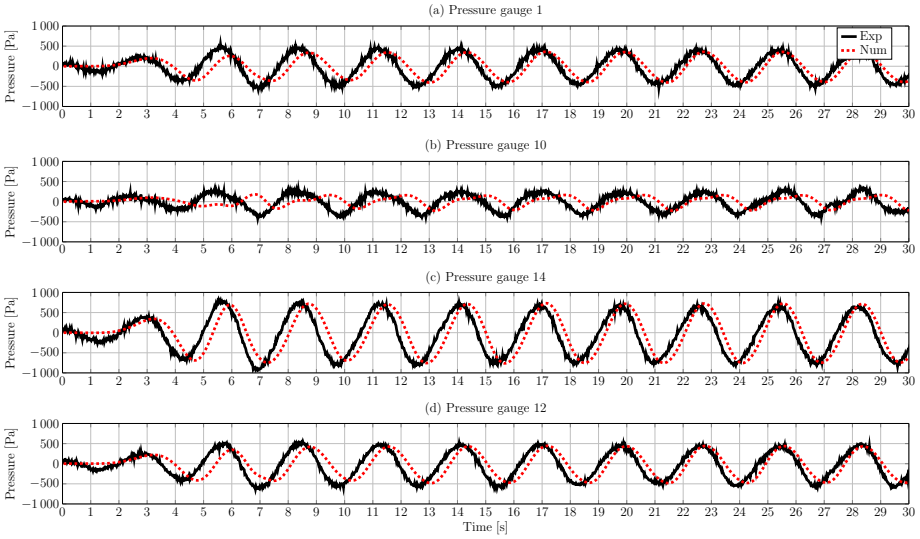

Figure 44: Numerical and experimental pressure data for sea state MS04 with experimental damping $D_{exp} = 200\text{N m s}$

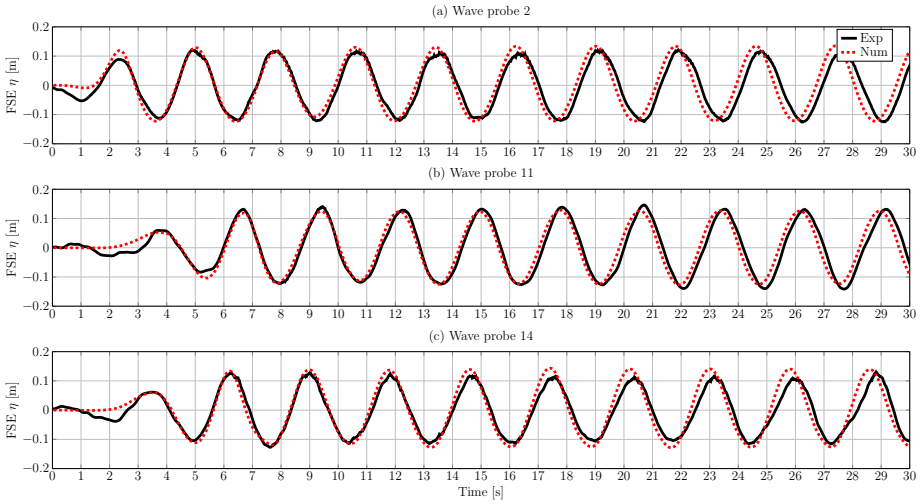

Figure 45: Numerical and experimental η data for sea state MS04 with experimental damping $D_{exp} = 200\text{N m s}$

6. Conclusion

This paper documents the validation of a 1:5 scale numerical model of the Wavestar device against experimental data under various test conditions. From the results, the following conclusions can be drawn:

- The system dynamics of the experimental setup can be captured with satisfying accuracy by introducing a linear spring-damper system in the CNWT, where coefficients are determined through linear least squares regression
- The validation of complex physical systems, such as the one on hand, is a challenging task and requires exact knowledge of all system characteristics. This detailed knowledge is difficult to acquire but is required for the formulation of assumptions for the numerical model. This may influence the achievable order of accuracy for validation studies.
- Given the required assumptions and simplification in the CNWT, the presented model of the Wavestar WEC is considered to be, in a general sense, validated
- The validated numerical model provides a powerful tool for future assessment of the power production of the Wavestar WEC under various conditions, avoiding costly and time consuming experimental tank tests.

Acknowledgment

This paper is based upon work supported by Science Foundation Ireland under Grant No. 13/IA/1886. Ed Ransley has been funded by the Engineering and Physical Sciences Research Council (EPSRC) via the SuperGen UK Centre for Marine Energy Research (UKCMER) as part of the third phase of the consortium's program of work (October 2011 - September 2016). Josh Davidson was supported by the Higher Education Excellence Program of the Ministry of Human Capacities in the frame of Water science & Disaster Prevention research area of Budapest University of Technology and Economics (BME FIKP-VZ). The experimental test campaign was funded by MARINET, a European Community Research Infrastructure Action under the FP7 Capacities Specific Programme. Additional acknowledge goes to the Danish ForskEL-programmes by Energinet.dk and partners in FLOAT2, "New Flexural UHPC Application for Wave Converters 2" and "Digital Hydraulic Power Take Off for Wave Energy".

References

[1] E. Ransley, D. Greaves, A. Raby, D. Simmonds, M. Jakobsen, M. Kramer, RANS-VOF modelling of the wavestar point absorber, Renewable Energy 109 (2017) 49–65.

[2] C. Windt, J. Davidson, J. Ringwood, Performance assessment of the overset grid method for numerical wave tank experiments in the OpenFOAM environment, in: Proceedings of the ASME 2018 37th International Conference on Ocean, Offshore and Arctic Engineering, 2018.

[3] C. Windt, J. Davidson, J. Ringwood, High-fidelity numerical modelling of ocean wave energy systems: A review of CFD-based numerical wave tanks, Renewable and Sustainable Energy Reviews 93 (2018) 610 – 630.

[4] J. Weber, Wec technology readiness and performance matrix–finding the best research technology development trajectory, in: Int. Conf. Ocean Energy Dublin Irel, 2012.

[5] M. Penabla, J. Davidson, C. Windt, J. Ringwood, A high-fidelity wave-to-wire simulation platform for wave energy converters: Coupled numerical wave tank and power take-off models, Applied Energy 226 (2018) 655–669.

[6] P. J. Roache, Quantification of uncertainty in computational fluid dynamics, Annual Review of Fluid Mechanics 26 (1997) 123–160.

[7] P. J. Roache, Verification and validation in computational science and engineering, Vol. 895, Hermosa Publisher Albuquerque, NM, 1998.

[8] J. Davidson, C. Windt, G. Giorgi, R. Genest, J. Ringwood, OpenFOAM : Selected papers from the 11th Workshop, Springer, 2018, Ch. Evaluation of energy maximising control systems for wave energy converters using OpenFOAM.

[9] C. Windt, J. Davidson, P. Schmitt, J. V. Ringwood, Assessment of numerical wave makers, in: Proceedings of the 12th European Wave and Tidal Energy Conference, Cork, Ireland, 2017.

[10] J. Davidson, S. Giorgi, J. V. Ringwood, Linear parametric hydrodynamic models for ocean wave energy converters identified from numerical wave tank experiments, Ocean Engineering 103 (2015) 31–39.

[11] J. Westphalen, D. M. Greaves, A. R., Z. Z. Hu, D. M. Causon, C. G. Mingham, P. Omidvar, P. K. Stansby, B. D. Rogers, Investigation of wave-structure interaction using state of the art CFD techniques, Open Journal of Fluid Dynamics 4 (2014) 18–43.

[12] P. Schmitt, B. Elsässer, The application of Froude scaling to model tests of Oscillating Wave Surge Converters, Ocean Engineering 141 (2017) 108–115.

[13] Z. Z. Hu, D. Greaves, A. Raby, Numerical wave tank study of extreme waves and wave-structure interaction using OpenFOAM, Ocean Engineering 126 (2016) 329–342.

[14] V. Mishra, S. Beatty, B. Buckham, P. Oshkai, C. Crawford, Application of an arbitrary mesh interface fo CFD simulation of an oscillating wave energy converter, in: Proceedings of the 11th European Wave and Tidal Energy Conference, Nantes, France, 2015.

[15] J. Palm, C. Eskilsson, G. M. Paredes, L. Bergdahl, Coupled mooring analysis for floating wave energy converters using CFD: Formulation and validation, International Journal of Marine Energy 16 (2016) 83–99.

[16] D. D. Prasad, M. R. Ahmed, Y.-H. Lee, R. N. Sharma, Validation of a piston type wave-maker using numerical wave tank, Ocean Engineering 131 (2017) 57–67.

[17] A. Elhanafi, G. Macfarlane, A. Fleming, Z. Leong, Scaling and air compressibility effects on a three-dimensional offshore stationary OWC wave energy converter, Applied Energy 189 (2017) 1–20.

[18] P. Schmitt, Investigation of the near flow field of bottom hinged flap type wave energy converters, Ph.D. thesis, School of Planning, Architecture and Civil Engineering, Queen's Univeristy Belfast (2013).

[19] Y. Wei, A. Rafiee, A. Henry, F. Dias, Wave interaction with an oscillating wave surge converter, Part I: Viscous effects, Ocean Engineering 104 (2015) 185 – 203.

[20] M. M. Jakobsen, S. Beatty, G. Iglesias, M. M. Kramer, Characterization of loads on a hemispherical point absorber wave energy converter, International Journal of Marine Energy 13 (2016) 1–15.

[21] G. Giorgi, M. Penalba, J. Ringwood, Nonlinear hydrodynamic models for heaving buoy wave energy converters, in: Proceedings of the 3rd Asian Wave and Tidal Energy Conference, Marina Bay Sands, Singapore, 2016.

[22] M. M. Jakobsen, Wave-Structure interations on point absorber, Tech. rep., Aalbor University Denmark (2014).

[23] R. Hansen, T. Andersen, H. Pedersen, Model based design of efficient power take-off systems for wave energy converters, in: Proceedings of the Twelfth Scandinavian International Conference on Fluid Power, Tampere, Finland, 2011.

[24] H. G. Weller, G. Tabor, H. Jasak, C. Fureby, A tensorial approach to computational continuum mechanics using object-oriented techniques, Computers in Physic 12 (6) (1998) 620 – 631.

[25] OpenFOAM Foundation, OpenFOAM 4.1 release notes, https://openfoam.org/download/4-1-ubuntu/ (2016).

[26] T. Holzmann, Mathematics, Numerics, Derivations and OpenFOAM, Holzmann CFD, 2016.

[27] S. Patankar, D. Spalding, A calculation procedure for heat, mass and momentum transfer in three-dimensional parabolic flows, International Journal of Heat and Mass Transfer 15 (1972) 1787–1806.

[28] R. I. Issa, Solution of the implicitly discretised fluid flow equation by operator-splitting, Journal of Computational Physics 62 (1986) 40–65.

[29] C. W. Hirt, B. D. Nichols, Volume of Fluid (VOF) Method for the Dynamics of Free Boundaries, Journal of Computational Physics 39 (1981) 201–225.

[30] E. Berberović, N. P. van Hinsberg, S. Jakirlić, I. V. Roisman, C. Tropea, Drop impact onto a liquid layer of finite thickness: Dynamics of the cavity evolution, Physical Review E 79 (2009) 036306–1 – 036306–15.

[31] R. Henrik, Computational fluid dynamics of dispersed two-phase flows at high phase fractions, Doctor Degree, Department of Mechanical Engineering, Imperial College London.

[32] C. Eskilsson, J. Palm, L. Bergdahl, On numerical uncertainty of VOF-RANS simulations of wave energy converters through V&V technique, in: Proceedings of the 12th European Wave and Tidal Energy Conference, Cork, Ireland, 2017.

[33] C. Windt, J. Davidson, E. Ransley, M. Jakobsen, M. K. amd J. V. Ringwood, Validation of a CFD-based numerical wave tank model of the wavestar ocean wave energy converter, in: Proceedings of the 3rd International Conference on Renewable Energies Offshore, Lisbon, Portugal, 2018.

[34] N. Jacobsen, D. R. Fuhrmann, J. Fredsoe, A wave generation toolbox for the open-source CFD library: OpenFoam(R), International Journal for Numerical Methods in Fluids.

[35] C. Windt, J. Davidson, P. Schmitt, J. Ringwood, A benchmark study for numerical wave makers in cfd simulations, submitted to Coastal Engineering.

[36] P. Higuera, J. L. Lara, I. J. Losada, Realistic wave generation and active wave absorption for NavierStokes models Application to OpenFOAM, Coastal Engineering.